Title	Numerical investigation of instability mechanism on thermo-solutal Marangoni convection in a liquid bridge under zero gravity
Author(s)	Agampodi Mendis, Radeesha Laknath
Citation	大阪大学, 2021, 博士論文
Version Type	VoR
URL	https://doi.org/10.18910/85416
rights	
Note	

Numerical investigation of instability mechanism on thermo-solutal Marangoni convection in a liquid bridge under zero gravity

RADEESHA LAKNATH AGAMPODI MENDIS

SEPTEMBER 2021

Numerical investigation of instability mechanism on thermo-solutal Marangoni convection in a liquid bridge under zero gravity

A dissertation submitted to

THE GRADUATE SCHOOL OF ENGINEERING SCIENCE

OSAKA UNIVERSITY

in partial fulfillment of the requirements for the degree of

DOCTOR OF PHILOSOPHY IN ENGINEERING

BY

RADEESHA LAKNATH AGAMPODI MENDIS

SEPTEMBER 2021

Abstract

The theoretical onset of the Marangoni convection instability occurring in a half-zone liquid bridge of the floating zone (FZ) growth of Si_xGe_{1-x} (SiGe) has been investigated by a newly developed method using global linear stability analysis (LSA) incorporated with direct numerical simulations (DNS). A half-zone model of a liquid bridge between cold and hot disks is considered. This study is focused on three main aspects, onset of thermo-solutal Marangoni convection in the case that the same direction of the thermal and solutal Marangoni forces, onset of thermo-solutal Marangoni convection in the case that the opposite direction of the thermal and solutal Marangoni forces, and flow instabilities in a liquid bridge of smaller aspect ratios.

In the case that the same direction of the thermal and solutal Marangoni forces, oscillatory disturbance patterns appear with different azimuthal wavenumbers for unstable eigenmodes. For pure thermal Marangoni convection in literature, the primary bifurcation is two-dimensional (2D) axisymmetric to a three-dimensional (3D) steady flow. On the other hand, the primary bifurcation in this study was 2D axisymmetric to a 3D oscillatory flow at the onset as increasing the thermal Marangoni number. The stability range of the present global LSA is consistent with the previous results on thermo-solutal Marangoni convection obtained by DNS.

The results were confirmed that the flow is 2D axisymmetric when the solutal Marangoni force is dominant when the thermal and solutal Marangoni forces are acting in opposite direction. The results reveal the hysteresis phenomena across thermal Marangoni numbers due to the coexistence of two stable flow solutions at the same thermal Marangoni number when thermal and solutal Marangoni convection coexists with opposing forces. The exactly predicted stability limits of FZ crystal growth by the newly developed method would be useful to avoid possible flow-induced disturbances and lead to the growth of single crystals without growth striations.

The effect of aspect ratio (A_s) of the liquid bridge on thermo-solutal Marangoni convection has been investigated by 3D numerical simulations. The A_s drastically affects the critical Marangoni numbers: the critical solutal Marangoni number has the same dependence on A_s as the critical thermal Marangoni number, i.e., it decreases with increasing A_s. The azimuthal wavenumber of the traveling wave mode increases as decreasing A_s but insusceptible of solutal Marangoni convection. The oscillatory modes of the hydro waves have been extracted as the spatiotemporal structures by using dynamic mode decomposition (DMD). The results suggest that the selection of the characteristic length of the Marangoni convection depends on A_s of the liquid bridge.

Contents

Chapter 1

Introduction

1.1 Background and motivation

Single crystals with high purity and quality are needed for the design of next-generation opto-electronic devices. Not only the Si_xGe_{1-x} (SiGe) alloy is the most prominent in the manufacturing process of solar cells, photodetectors, thermoelectric power generators, high-speed temperature sensors, bipolar junction transistors, and field effect transistors but also the quality and the performance of these devices depend on the quality of SiGe single crystals. Therefore, the availability of high quality, relatively defect and impurity-free, and compositionally uniform SiGe substrates is desirable. To achieve high quality SiGe crystals a variety of melt crystal growth techniques such as Floating zone, Czochralski and open boat have been utilized [1–8]. Each of these techniques has its issues such as crystal compositional uniformity, crucible contamination, the need of seed, etc. Among those, the floating zone (FZ) method offers growth of high quality, contamination free SiGe crystals since the growth is achieved without using a crucible (it is a container-less technique). The absence of a growth crucible prevents possible crucible contamination and gives rise to the growth of more homogeneous and purer crystals. However, the presence of a free-surface (the melt-gas interface) in this technique gives rise to thermal and solutal Marangoni flows in the growth melt (liquid bridge) along its free surface due to the variation of surface tension. Such flows in the liquid bridge induce flow velocity fluctuations that may lead to unstable and non-uniform growth [9]. Therefore, the effects and relative contributions of these flows on the growth process need to be examined. In FZ experiments, because of gravity, the size of crystals to be grown is limited. In addition, a strong buoyancy-driven natural convective flow develops in the melt. This strong flow may not only affect crystal quality adversely, but also make it difficult to determine the effects and relative contributions of Marangoni convection to the growth process and crystal quality. Thus, in order to determine the effects of Marangoni convection it is customary to carry out numerical simulations under no gravity. In order to minimize these adverse effects of gravity, FZ experiments have also been carried out under microgravity. For instance, it was shown that the microgravity environment may help minimize the adverse effect of natural convection and offer quiescent, diffusion-limited growth which minimizes undesirable striations [10]. However, it was shown that even under microgravity, that, as predicted, Marangoni convection may induce undesirable growth striations into grown crystals [11–13]. Such growth striations observed in the FZ growth process are caused by the fluctuations of Marangoni flow velocity (time-dependent flow oscillations) in the melt. Thus, capturing the essential and relevant hydrodynamics of the FZ growth molten zone is of utmost importance for a better understanding of the effects of Marangoni convection in minimizing possible undesirable growth striations. Since the semiconductor melts are opaque, in-situ visualization of flow structures in FZ experiments is not possible. In FZ growth, the thermal Marangoni convection is normally dominant for semiconductor melt such as Si. However, the alloy of SiGe shows a significant difference since surface tensions of Si and Ge are very different. Such a difference of surface tension also gives rise to a stronger solutal Marangoni convection along with the thermal Marangoni convection in the SiGe melt. This aspect also makes interesting to study the FZ growth of SiGe alloy system.

1.1.1 The floating zone method

During the process of the floating zone method, a floating melt zone is grooved by surface tension between the polycrystalline feed rod and the grown single crystal (see Figure 1.1). The melt zone is locally heated by a ring-type heater as shown in Figure 1.1. This floating melt zone is slowly moved relative to the heating device along the rod and the crystal grows right below the melt zone on the seed rod. In this method, the melt zone between feed and seed rod is stabilized only by surface tension. Therefore the molten zone does not need to be in contact with a crucible which avoids the contamination and nucleation at the lateral boundary and allows the formation of perfect and more pure crystals.

In a container-less technique, massive samples can only be processed in microgravity environments. On the Earth conditions, the floating zone configuration tends to deform

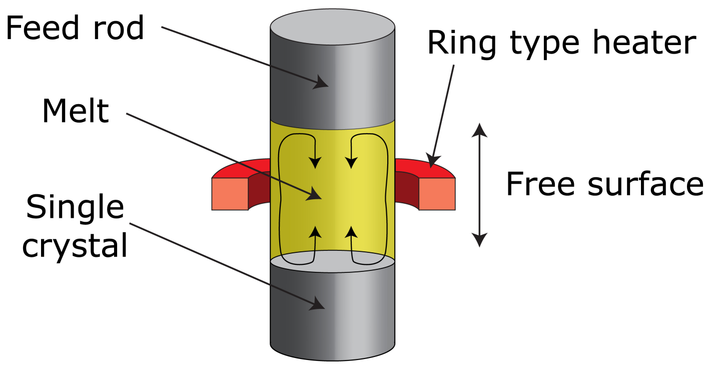

FIGURE 1.1: Floating zone method

due to its weight and this effect limits the zone height. The development of the technology to access the microgravity environments makes feasible the floating zone experiments with greater zone heights. Although the natural convection eliminates from the floating zone method due to the microgravity conditions, Marangoni flow driven by the temperature and concentration gradients acting along the axial direction of the liquid bridge causes undesirable composition variations (striations) into grown crystals [14, 15].

1.1.2 Numerical modeling

Numerical modeling of the floating zone method has become an advantageous technique with the development of computer hardware performance in very recent years [16–18]. Moreover, the efficiency of computational algorithms has been improved by paralleling the improvement in computer hardware. Experiments on the floating zone method could only be carried out for transparent liquids as the convection patterns are not visible in opaque fluids. Most of the semiconductor melts are low Prandtl number opaque fluids. The cost of performing experiments in space is very high as the preparation of such experiments needs great accuracy. All these factors combined to make numerical simulations inexpensive and power full tool in contrast to performing experiments in space or ground-based microgravity laboratories.

Over the years, the half zone configuration has become a very important "paradigm" model for fundamental research on the floating zone method due to its simplicity and less computational cost. In this model, the flow in a half of the real floating zone simulates by assuming the flow is symmetric by reflection about the middle plane between seed and feed

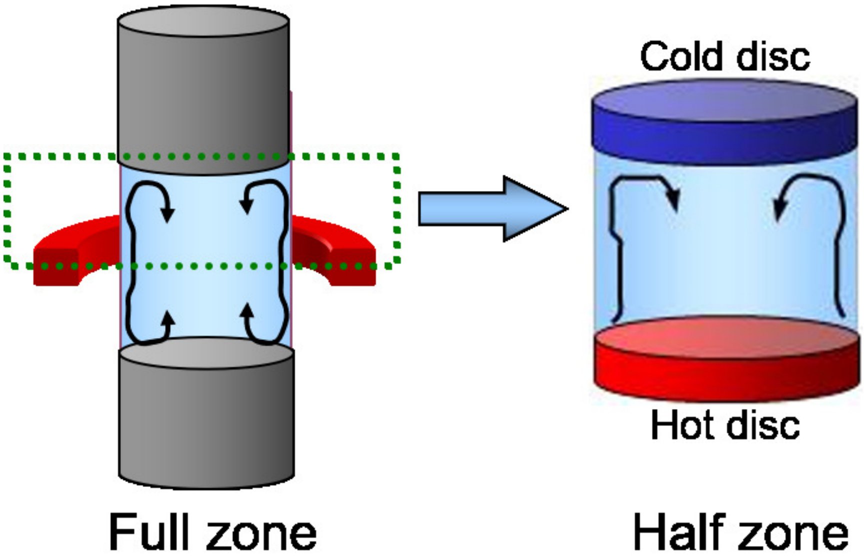

FIGURE 1.2: Configuration of half zone model

rods. The no-slip condition applies on this symmetric plane does not affect the flow dynamics. Specified heat flux distribution is applied on the free surface with a maximum of the flux imposed at the equatorial plane by holding the maximum and minimum temperatures at the end disks of the half zone model, as shown in Figure 1.2. Surface tension forces drive a flow along the free surface from hot disk to cold one generating a single toroidal vortex [14].

1.1.3 Objectives

In the past, the instabilities of Marangoni convection in the half-zone liquid bridge have been analyzed over different configuration ratios from one to two dimensional by either experiments or numerical simulations. The majority of these researches focus on the high Prandtl number fluids and considered only pure thermal Marangoni convection [17, 19–22]. But some recent publications have shown the solutal Marangoni convection also significantly affects the flow structure in the floating zone method [23, 24]. This leaves the onset of the thermo-solutal Marangoni convection still an open question in a half zone liquid bridge under zero gravity. The numerical simulation is a powerful tool for solving this but, numerical simulation results highly depend on the numerical method, discretization scheme, discretization order, grid refinement. etc.

To understand the Marangoni convection flow in the floating zone technique it is necessary to find the critical Marangoni number which is independent of the initial conditions by considering both solutal and thermal Marangoni convection. The present study is in an attempt to fill the gaps of low Prandtl number three-dimensional thermo-solutal Marangoni convection in literature. The goal of this thesis is to develop a new method for the exact prediction and clarification of instability of thermo-solutal Marangoni convection in a half-zone liquid bridge under zero gravity.

1.2 Other research background related to this research

As mentioned earlier the FZ technique being a container-less growth method has the advantage of growing high purity crystals over other crystal growth techniques. However, it also has challenges. First, the materials used have high melting points and are opaque for situ observations. This presents difficulties in experiments. Secondly, the size of the liquid bridge is limited due to the gravity on Earth. This prevents the growth of larger crystals. The growth of larger crystals is only possible under microgravity conditions. However, the possibility of microgravity experiments is very rare and in addition such experiments are very expensive. Thus, numerical simulation studies under either micro- or zero-gravity conditions present themselves as very viable and inexpensive alternatives to study various aspects of the FZ growth technique [15]. In these simulations mostly the half-zone model is adopted for computational efficiency by considering the half of the full-zone liquid bridge. The half zone configuration is characterized by a single toroidal vortex developed between hot and cold disks of the zone.

1.2.1 Numerical simulations

Literature in this area is relatively well-developed. For instance, experiments and numerical simulations (see for instance [17, 25–36]) performed with high-Prandtl-number fluids considering pure thermal Marangoni convection showed that the flow in the liquid bridge is laminar, steady and axisymmetric for sufficiently small thermal Marangoni numbers, but when the thermal Marangoni number exceeds a particular threshold, flow show oscillatory three-dimensional (3D) flow patterns. For low Prandtl number fluids (semiconductor melts), the steady flow breaks the axisymmetry and becomes a 3D-steady flow regime (stationary bifurcation) before the onset of a 3D oscillatory flow (Hopf bifurcation) (see, for instance, [17, 37–42]). The direct numerical simulations (DNS) [23, 24, 43] on thermo-solutal Marangoni convection in literature have shown that not only thermal Marangoni convection, but also solutal Marangoni convection significantly contributes to the flow structures in the liquid bridge of the FZ method [23, 24, 43–45]. When considering the combined effects of thermal and solutal Marangoni convections for low Prandtl number fluids, the axisymmetric steady flow bifurcates to 3D oscillatory with the absence of a stationary bifurcation depending on the thermal and solutal Marangoni numbers values.

The stability of Marangoni convection in a liquid bridge under zero gravity has been the subject of researches in recent years. These studies suggest that flow instability in such configurations may be responsible for the undesirable defects that appear in crystals grown by floating zone methods, even under conditions of microgravity and normal gravity [46–50]. However, very few works appeared in the literature related to the instability analysis of Marangoni flow in the floating zone method, and many of these studies [51–60] were based on the simplifying assumption of axisymmetric flow. Therefore, due to the experimental findings of the existence of three-dimensional complex flow states, the role of nonaxisymmetric disturbances needs to be further investigated. The direct numerical solutions of the nonlinear and time-dependent Navier–Stokes equations by [19, 61, 62] show that the first bifurcation is stationary for liquid metals and the flow regime becomes oscillatory only when the Marangoni number is further increased. However, the information dealing with fundamental properties of Marangoni flow instability and three-dimensional flow patterns are showing a great lack in literature. Nevertheless, the instability of the first bifurcation steady to three-dimensional flow may play an important role in the floating zone crystallization process. This has been proved by experimental studies and some numerical simulations [63].

1.2.2 Linear stability analysis

In addition to DNS, linear stability analysis (LSA), proper orthogonal decomposition (POD), and dynamic mode decomposition (DMD) are some useful techniques to investigate the hydrodynamic processes. The LSA has been used ([39, 40, 42, 64–66]) to find the onset of thermal Marangoni convection by assuming specific forms of perturbation due to the limitation of computational cost. The development of mathematical frameworks yields the global LSA technique which computes the three-dimensional instability modes by using Arnoldi iteration ([67]) incorporated with time-stepping DNS solver as in recent previous studies (see for instance [68–70]). In this method, the three-dimensional instability modes are calculated by solving an eigenvalue problem for 3D perturbation. Approximated eigenvalues and eigenfunctions were found by constructing the orthonormal basis of Krylov subspace to overcome the problem of solving the large Jacobian matrix of the right-hand side of the linearized Navier–Stokes equations (the order of dimensions of freedom is more than $O(10^6)$).

1.2.3 Dynamic mode decomposition

DMD is also a leading technique in analyzing the spatio-temporal flow patterns in transitional regimes. The POD extracts a hierarchical set of orthogonal spatial modes ranked according to their contribution to the total energy of flow modes. The POD is much suitable, therefore, for extracting the statistical structures from a complex flow. In comparison, DMD assumes physically more relevant modes to the oscillatory growth and decay in time. DMD is an emerging data-driven technique to obtain linear reduced-order models for high-dimensional complex systems. In addition to linear reduced-order models, the spatial-temporal coherent structures or patterns that dominate the observed measurement data from that dynamical system can also be extracted by DMD. This is initially introduced in the fluid dynamics community by Schmid [71], and it has later been connected to this nonlinear dynamical systems theory called Koopman theory by Rowly et al.[72]. This technique comes out of the fluid mechanics community, but since then, DMD has been applied to a broad range of systems, including disease modelling, neuroscience, robotics and finance [73–77]. Part of the reason for the broad application of DMD is that it is pure data-driven and does not require any description of underlying governing equations. It can be used as a post-processing tool for analyzing the spatio-temporal structures of experimental data.

3D flow structures are developing inside the liquid bridge floating zone system due to Marangoni convection. Investigation of the flow dynamics of those structures is a vital requirement for producing defect-free crystals. Since the 3D time snapshots by numerical simulations alone do not help to understand the hydrodynamic process, the DMD is giving a proper understanding of the dynamical system.

1.2.4 Invarient solutions

A numerical simulation study on the characterization of thermo-solutal Marangoni convection convection driven by opposite Marangoni forces was carried out by [78]. In their study, the flow transitions were complex, and different flow regimes (steady axisymmetric,3D steady, 3D oscillatory and Chaotic) developed depending on the Marangoni number values. However, a theoretical investigation of the "onset" of thermo-solutal Marangoni convection driven by opposing forces is also absent in the literature. The flow states that keeping the flow behavior exactly the same under some disturbances are known as "invariant solutions", recurrent flows, or periodic orbits. Such solutions are important for the understanding of the basic physics behind the flow phenomena we observe since the DNS results depend on the initial conditions. Recently, however, the Newton-Krylov method has been used in several flow systems to find invariant solutions and their stable and unstable manifolds ([79]). In this technique, the process of finding exact flow solutions is reduced to a simple optimization exercise starting from an initial condition (i.e. an arbitrary flow snapshot) calculated by a DNS solver. In each iterative step, a new solution is obtained by the aforementioned Arnoldi iteration method. This algorithm is repeated until the relative error between current and previous flow states satisfies a stopping criterion.

1.2.5 The effect of geometrical aspect ratio

Numerical results of Lappa et al.[80] have confirmed the existence of different behaviors of Marangoni flows exist depending on the Prandtl number and the geometrical aspect ratio of the liquid bridge. A detailed study of the linear stability analysis for low Prandtl number fluids by Wanschura et al. [40] has found the modes with higher azimuthal wave numbers critical as the aspect ratio decreases. Similar relationships between the aspect ratio of the liquid bridge and wavenumbers for high-Prandtl numbers have also been observed experimentally (see, for instance, [81]). A parametric analysis of the influence of the aspect ratio of the full zone can also be found in literature [14, 82]. The assumption of the full zone model is the only way to capture in detail the mechanism of the instability of Marangoni flow generating in the real floating zone is one of the advantages of the full zone model. They have concluded that the critical wavenumber increases if the geometrical aspect ratio decreases but the critical Marangoni number does not change much with the aspect ratio. However, the full zone model has a disadvantage in that the temperature at the equatorial cross section cannot be fixed due to convective and heat transfer mechanisms establishing the temperature difference which is driving the surface flow. In the half zone model, on the other hand, the temperature difference can be fixed by holding maximum and minimum temperatures at the end disks. The no-slip condition imposed on the symmetric plane at the mid-height between the rods of the real floating zone makes the flow dynamics of the half zone model much closer to the real floating zone. Thus, the half zone model has become a very important and computationally inexpensive paradigm model for fundamental research. These studies show that the geometrical aspect ratio of the liquid bridge is as critical as the Marangoni numbers for the thermo-solutal Marangoni flow developing in the liquid bridge. To the best of our knowledge, the dependency of flow regimes on the aspect ratio of the liquid bridge when the thermal and solutal Marangoni convections are co-existing is still unknown in the literature.

The above review justifies the development of a new method incorporating DNS with LSA and DMD is a vital requirement for the exact prediction of instability of thermo-solutal Marangoni convection in a half-zone liquid bridge under zero gravity.

1.3 Thesis outline

This thesis consists of five chapters. In the first chapter, the background and motivation of the research is introduced and previous research works related to experimental and numerical studies on Marangoni convection in the floating zone liquid bridge are reviewed.

In the second chapter, the configuration of the numerical model and governing equations are presented.

The third chapter discussed the theoretical details of global linear stability analysis (LSA), dynamic mode decomposition (DMD) and the validation of LSA code.

The results obtained during the current study are presented and discussed in the chapters four to six.

The seventh chapter summarized and concluded this thesis. Future works are also discussed in this chapter. In Appendices, we introduce the software used in our calculations and briefly describe the discretization method for the governing equations and mathematical algorithm used for computations.

Chapter 2

Configuration and governing equations

2.1 Configuration of the numerical model

The model of a half-zone liquid bridge between two parallel concentric cold and hot disks of radius a with a distance L apart (Figure 2.1) is adopted. The aspect ratio of the liquid bridge is defined as $A_s = L/a$.

Assumptions:

(i) The liquid surface is non-deformable, cylindrical and adiabatic.

(ii) The melt (a mixture of Silicon and Germanium) is an incompressible and Newtonian fluid.

(iii) The system is under zero gravity, thus the liquid bridge keeps its cylindrical shape since we assume zero gravity.

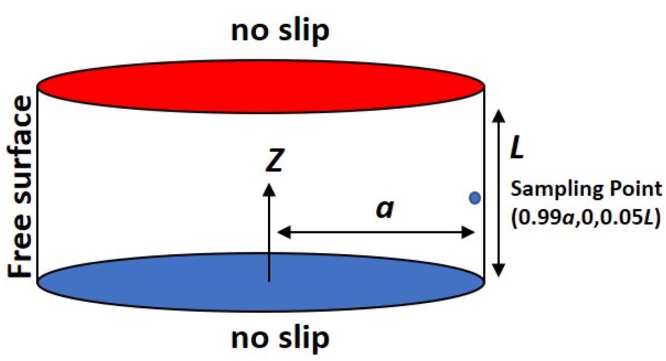

FIGURE 2.1: Geometry of a half zone liquid bridge system.

2.2 Governing equations

The non-dimensional governing equations of the melt are obtained from the overall conservation of mass, the balance of momentum, the balance of energy, and the conservation of species mass,

$$
\begin{aligned}
\boldsymbol{\nabla} \cdot \boldsymbol{u} &= 0 && (2.1)\\
\frac{\partial \boldsymbol{u}}{\partial t} + \boldsymbol{u} \cdot \boldsymbol{\nabla} \boldsymbol{u} &= -\boldsymbol{\nabla} p + \nabla^2 \boldsymbol{u} && (2.2)\\
\frac{\partial T}{\partial t} + \boldsymbol{u} \cdot \boldsymbol{\nabla} T &= \frac{1}{Pr} \nabla^2 T && (2.3)\\
\frac{\partial C}{\partial t} + \boldsymbol{u} \cdot \boldsymbol{\nabla} C &= \frac{1}{Sc} \nabla^2 C && (2.4)
\end{aligned}
$$

where the coordinates (r, θ, z) and time t are, hereafter, nondimensional, and $\boldsymbol{u} = (u_r, u_\theta, u_z)$, p, T and C denote the dimensionless flow velocity, pressure, temperature and silicon concentration, respectively. The associated field variables namely flow velocity vector $\boldsymbol{u} = (u_r; u_\theta; u_z)$, temperature T, and the melt Si concentration C are nondimensionalized with respect to the characteristic variables of length L_c, time L_c^2/ν, velocity ν/L_c, temperature difference ΔT and concentration difference ΔC (between top and bottom walls) where $\nu(= \mu/\rho)$ is the kinematic viscosity given in terms of melt density ρ and melt viscosity μ. The associated Schmidt and Prandtl numbers are defined by $Sc = \nu/D$ and $Pr = \nu/\alpha$, where α and D represent, respectively, the melt thermal diffusivity and the diffusion coefficient of Si in the melt.

The characteristic length is chosen as $L_c = L$ when the study is carried out by keeping the aspect ratio of the liquid bridge as a constant in chapter 4.2 and chapter 4.3. In chapter 4.4 since the three different aspect ratios are considered according to three different L values and therefore, the characteristic length is chosen as $L_c = a$.

2.2.1 Boundary conditions

The boundary conditions on the walls are non-slip ($\boldsymbol{u} = 0$) for flow velocity components. When considering the case of the thermal and solutal Marangoni forces are in the same direction (chapter 4.2 and chapter4.4), the top cold disk surface ($z = A_s$) has $T = 0$ and $C = C_{Si} = 1$ and, the bottom hot disk surface ($z = 0$) has $T = 1$ and $C = 0$. When considering the case of the thermal and solutal Marangoni forces are in opposite direction (chapter 4.3), the top hot disk surface ($z = 1$) is at $T = 1$ and $C = C_{\mathrm{Si}} = 1$, and the bottom cold disk surface ($z = 0$) is at $T = 0$ and $C = 0$.

These boundary conditions along the free surface are

$$u_r = 0 \tag{2.5}$$

$$r^2 \frac{\partial}{\partial r}\left(\frac{u_\theta}{r}\right) = Ma_{\mathrm{T}}\left|\frac{\partial T}{\partial \theta}\right| + Ma_{\mathrm{C}}\left|\frac{\partial C}{\partial \theta}\right| \tag{2.6}$$

$$\frac{\partial u_z}{\partial r} = Ma_{\mathrm{T}}\left|\frac{\partial T}{\partial z}\right| + Ma_{\mathrm{C}}\left|\frac{\partial C}{\partial z}\right| \tag{2.7}$$

$$\frac{\partial T}{\partial r} = 0, \quad \frac{\partial C}{\partial r} = 0 \tag{2.8}$$

The Ma_{T} and Ma_{C} are the thermal and solutal Marangoni numbers, respectively, which represent the magnitude of the surface tension relative to the viscous force,

$$Ma_{\mathrm{T}} = \left(\frac{\partial \sigma}{\partial T}\right)\frac{\Delta T L_c}{\mu \nu}, \quad Ma_{\mathrm{C}} = \left(\frac{\partial \sigma}{\partial C}\right)\frac{\Delta C L_c}{\mu \nu}, \tag{2.9}$$

where $\partial\sigma/\partial T(< 0)$ and $\partial\sigma/\partial C(> 0)$ are the surface tension coefficients of the temperature and concentration fields, respectively.

The grid resolution used in chapter 4.2 as $N_r \times N_\theta \times N_z = 30 \times 120 \times 40$ and in chapter 4.3 and chapter 4.4 as $N_r \times N_\theta \times N_z = 40 \times 160 \times 60$. The details of the non-uniform grid refinement, numerical schemes, and the validation of transient OpenFOAM solver can be found in previous study [83]. The physical properties of $\mathrm{Si}_x\mathrm{Ge}_{1-x}$ liquid bridge are from Abbasog et al. [84]: the kinematic viscosity $\nu = 1.4 \times 10^{-7}\mathrm{m}^2/\mathrm{s}$, the thermal diffusivity $\alpha = 2.2 \times 10^{-5}\mathrm{m}^2/\mathrm{s}$, the diffusion coefficient $D = 1.0 \times 10^{-8}\mathrm{m}^2/\mathrm{s}$, which corresponds to $Pr = 6.37 \times 10^{-3}$ and $Sc = 14$.

Chapter 3

Numerical methods

3.1 Global linear stability analysis

Global linear stability analysis (LSA) theory has been revealed to play an important role in the investigation of physical mechanisms behind the laminar flow in complex geometries through a transition to turbulence [68, 70, 85, 86]. The theory serves the temporal and spatial evaluation of the growth rate of infinitesimal amplitude perturbations superimposed with a steady or periodic laminar base flow. Asymptotic instability of such perturbations can be obtained by a generalized large-scale eigenvalue problem that contains growth/damping rates and modal frequencies. This large-scale eigenvalue problem can be solved numerically by a matrix-forming strategy which can access to a full spectrum of eigenvalues. This matrix-forming framework required large computational memory (RAM). This is because the Jacobian matrix of the right-hand side of the linearized Navier-Stokes equation is huge (the order of dimensions of freedom is more than $O(10^6)$) due to the three-dimensional geometry. To overcome this problem subspace projection-iterative method such as Arnoldi iteration [67, 69] has been used in recent previous studies to find approximated eigenvalues and eigenfunctions by constructing the orthonormal basis of Krylov subspace [87–89]. In this matrix-free/Jacobian-free framework, the leading eigenvalues (eigenvalues with largest real-part) can be accurately calculated with the reduced order of dimension, O(10–100). The Stability of a base flow can be predicted based on the real part of the leading eigenvalue. The real part of the leading eigenvalue gives the growth /decay rate of the infinitesimal amplitude perturbations superimposed with the base flow.

In this method, the melt flow is decomposed into a base flow $(\overline{\boldsymbol{u}}, \overline{T}, \overline{C})$ and three dimensional infinitesimal perturbations ($\epsilon \boldsymbol{u}'$, $\epsilon T'$, $\epsilon C'$) with $\epsilon \ll 1$,

$$\boldsymbol{u}(r,\theta,z,t) = \overline{\boldsymbol{u}}(r,\theta,z) + \epsilon \boldsymbol{u}'(r,\theta,z,t) \tag{3.1}$$

$$T(r,\theta,z,t) = \overline{T}(r,\theta,z) + \epsilon T'(r,\theta,z,t) \tag{3.2}$$

$$C(r,\theta,z,t) = \overline{C}(r,\theta,z) + \epsilon C'(r,\theta,z,t) \tag{3.3}$$

where $(\cdot)'$ represents the normalized perturbation (i.e. the L_2 norm is $||\boldsymbol{u}'|| = 1$, $||T'|| = 1$, and $||C'|| = 1$). A linearized eigenvalue problem can be obtained by substituting eqs. (3.1)–(3.3) into the governing equations eqs. (2.1)–(2.4) and by ignoring the second-order infinitesimal terms. We rewrite the governing equations in terms of variable $\boldsymbol{x} = (\boldsymbol{u}, T, C)$ as

$$\frac{\partial \boldsymbol{x}}{\partial t} = f(\boldsymbol{x}) \tag{3.4}$$

and the governing equation in terms of $\boldsymbol{x}'$ is expressed as

$$\frac{\partial \boldsymbol{x}'}{\partial t} = \frac{\partial f(\overline{\boldsymbol{x}})}{\partial \overline{\boldsymbol{x}}} \boldsymbol{x}' = \boldsymbol{A}\boldsymbol{x}' \tag{3.5}$$

where $\boldsymbol{A}$ is the Jacobian matrix. The growth rate λ of the infinitesimal perturbation $\boldsymbol{x}'$ (= $\widehat{\boldsymbol{x}}(r,\theta,z)\exp(\lambda t)$) can be obtained by solving the eigenvalue problem as

$$\lambda \widehat{\boldsymbol{x}} = \boldsymbol{A}\widehat{\boldsymbol{x}} \tag{3.6}$$

The real part of λ determines the stability of the base flow ($\overline{\boldsymbol{x}}$) with respect to the infinitesimal perturbations: unstable, $\Re(\lambda) > 0$; neutral, $\Re(\lambda) = 0$; stable, $\Re(\lambda) < 0$. While the non-zero imaginary part of λ indicates the oscillation of the perturbation. The growth rate λ depends on Ma_{T} and Ma_{C} The Marangoni number at $\Re(\lambda) = 0$ gives the onset (critical) value, and the corresponding eigenfunctions ($\widehat{\boldsymbol{x}}$) represent an instability mode with respect to the base flow considered ($\overline{\boldsymbol{x}}$).

The generalized eigenvalue problem of eq. (3.6) can be solved by Arnoldi method combined with unsteady solve as shown in Appendix B. The base flow, $\overline{\boldsymbol{x}}$, has been calculated at each Marangoni number using a steady-state solver of OpenFOAM. The difference between the calculated flow fields of transient solver and that of the steady solver is the order of magnitude of O(10^{-5}). which is less than the perturbation magnitude used in the present study.

3.2 Dynamic mode decomposition

Dynamic information and coherent structures are significant in an investigation of fluid flow instability mechanisms. The Dynamic Mode Decomposition (DMD) theory introduced by [71] has been used in many recent studies to extract dynamic mode information from complex flow fields. This approach was originally invented as a post-processing tool for experimental and numerical data. The dynamic mode decomposition is a data processing method originally developed in the fluid dynamics community which takes large data sets typically velocity vorticity fields in time of a fluid simulation or a fluid experiment. This method provides a spatial and temporal decomposition of this data into dynamic modes that are spatially coherent and oscillate at a fixed frequency in time. For linear dynamical systems, these modes are analogous to global linear stability modes [72, 90–92]. Although this technique was invented for the fluid dynamic community, DMD has been applied to many systems such as neuroscience, finance, robotics, and disease modeling [93–101]. The major reason for such broad application of DMD is that it does not need to solve any nonlinear governing equations and can be used as a post-processing tool for analyzing numerical as well as experimental data. In the liquid bridge floating zone system, three-dimensional flow structures develop due to the Marangoni convection. The numerical simulation data of the liquid bridge system alone does not help to understand the hydrodynamic process properly. The DMD essentially gives a coupled system of spatial temporal modes, and recently used to extract an approximate periodic system from unknown data samples. The Marangoni convection along the free surface of the liquid bridge gives rise to the development of periodic flow structures and DMD is useful to analyze the dynamical behaviour of such structures.

A temporal sequence of data snapshots from numerical simulation are given by a matrix $\boldsymbol{X}_1^N$,

$$\boldsymbol{X}_1^N = \{\boldsymbol{x}_1, \boldsymbol{x}_2, \boldsymbol{x}_3, ..., \boldsymbol{x}_N\} \tag{3.7}$$

where $\boldsymbol{x}_i$ denotes the i–th flow field ($N = 1, 2, 3, ..., N$). A constant sampling time Δt of the data sequence is chosen according to the Nyquist criterion (see [71] in details). A linear mapping $\boldsymbol{A}$ between a flow field $\boldsymbol{x}_i$ and the subsequent flow field $\boldsymbol{x}_{i+1}$ is

$$\boldsymbol{x}_{i+1} = \boldsymbol{A}\boldsymbol{x}_i \tag{3.8}$$

which is considered as a linear approximation of solving the governing equations. The dynamic characteristics of the system is given by the eigenvalues and eigenvectors of the matrix $\boldsymbol{A}$. Furthermore, Eq. (3.8) can be written in the matrix form

$$\boldsymbol{X}_2^N = \boldsymbol{A}\boldsymbol{X}_1^{N-1} + \boldsymbol{r}\boldsymbol{e}_{N-1}^T \tag{3.9}$$

where $\boldsymbol{r}$ is the residual vector and $\boldsymbol{e}_{N-1} \in \mathbb{R}^{N-1}$. The singular value decomposition (SVD) is applied since SVD is robust to numerical errors and noises in the data. Substituting the SVD of $\boldsymbol{X}_1^{N-1}(= \boldsymbol{U}\boldsymbol{\Sigma}\boldsymbol{W}^H)$ into eq. (3.9), then

$$\boldsymbol{U}^H\boldsymbol{A}\boldsymbol{U} = \boldsymbol{U}^H\boldsymbol{X}_2^N\boldsymbol{W}\boldsymbol{\Sigma}^{-1} \equiv \tilde{\boldsymbol{A}} \tag{3.10}$$

with $\boldsymbol{U}$ contains the proper orthogonal modes of $\boldsymbol{X}_1^{N-1}$. Since the $\boldsymbol{A}$ related to $\tilde{\boldsymbol{A}}$ via a similarity transformation, the dynamic modes Φ_i can be expressed as

$$\Phi_i = \boldsymbol{U}\boldsymbol{y}_i \tag{3.11}$$

where $\boldsymbol{y}_i$ is the i–th eigenvector of $\tilde{\boldsymbol{A}}$, i.e. $\tilde{\boldsymbol{A}}\boldsymbol{y}_i = \mu_i\boldsymbol{y}_i$. The logarithmic transform of μ_i,

$$\lambda_i = \log(\mu_i)/\Delta t \tag{3.12}$$

represents the stability of extracted dynamics oscillatory mode, where, the real part of the eigenvalues, $\Re[\lambda]$, represents the growth/decay rate, and the imaginary part, $\Im[\lambda]$ does the frequency (wavelength) of each mode. For each case, 250 snapshots of the instantaneous concentration fields with a sampling rate $\Delta t = 2$ were processed in the present study using the DMD algorithm.

3.3 Model validation

The validation of linear stability analysis code has been done by comparing the first critical thermal Marangoni numbers from the literature [39, 40] for two different low Prandtl number values 0.02 and 0.01 with the aspect ratio of $A_s = 1$. As summarized in Table 6.1, the critical thermal Marangoni numbers obtained from the present linear stability code agree with the critical Reynolds numbers of the literature within 1%. The definitions of the thermal Marangoni number of the present study and that of the Reynolds number of the literature are the same. In this study the Krylov subspace dimension $k = 20$ is sufficient to use for the recovery of the three first leading eigenvalues.

TABLE 3.1: Comparison of the critical thermal Marangoni numbers with [40].

Pr	A_s	Ref.	Present
0.01	1	1899	1887
0.02	1	2062	2041

Chapter 4

Onset of thermo-solutal Marangoni convection when the same direction of the thermal and solutal Marangoni forces

A global linear stability analysis has performed to determine the onset of thermo-solutal Marangoni convection in the half-zone liquid bridge of the FZ growth of Si_xGe_{1-x} under zero-gravity when the thermal and solutal Marangoni forces are acting in the same direction.

Figure 4.1 shows the stability diagram of the axisymmetric base flow together with previous DNS results (on thermosolutal Marangoni convection) of [45]. For a certain Ma_{T}, when Ma_{C} increases, the real part of the leading eigenvalue becomes positive, which indicates that the steady axisymmetric ($m = 0$) flow (base flow) becomes unstable.

Figure 4.2 presents an example of the eigenvalue spectrum at $Ma_{\mathrm{T}} = 1750$ (and Ma_{C} $= 917$ and 928) near the onset of thermosolutal Marangoni convection. The critical $Ma_{\mathrm{C}} =$ $922.5 \pm 0.6\%$

Figures 4.3 and 4.4 show the vertical velocity disturbances of normalized eigenfunctions corresponding to the least stable mode and concentration patterns obtained by DNS, respectively.

The azimuthal waves of the unstable modes are observed distinctly in Fig. 4.3 and the wavenumbers are $m = 3$, 4, 5, 6, and 7 depending on Ma_{T} and Ma_{C}. The concentration patterns obtained by DNS are consistent with the patterns of most unstable modes by LSA. All primary bifurcations are from 2D axisymmetric to oscillatory modes except for the case $Ma_{\mathrm{C}} = 0$ for the range of thermal and solutal Marangoni numbers considered in the present study.

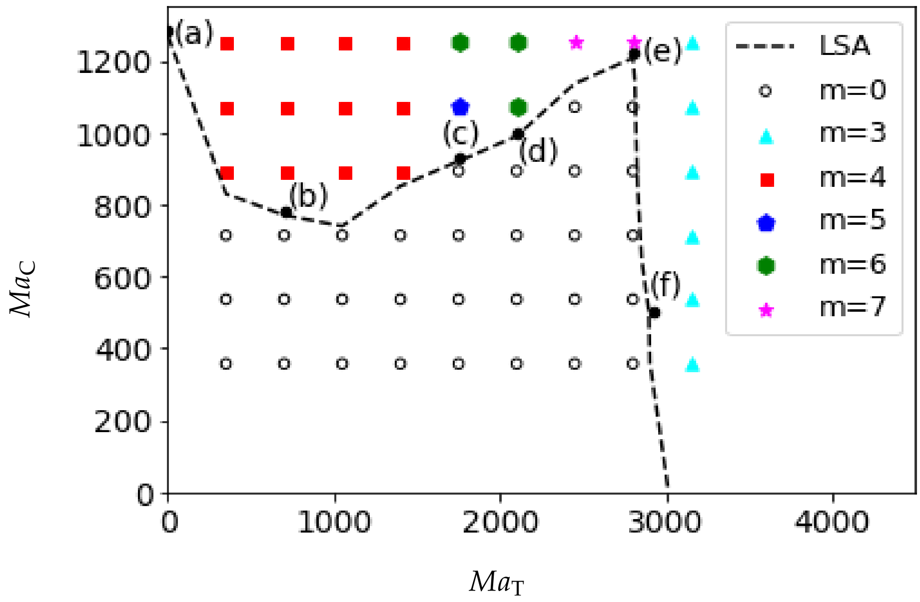

FIGURE 4.1: Stability diagram of the axisymmetric base flow in (Ma_T, Ma_C) (dashed line) together with previous DNS results of [45] at $Pr = 6.37 \times 10^{-3}$, $Sc = 14$, $A_s = 0.5$. The cases (a-f) are shown in Figs. 4.3 and 4.4.

For the thermal Marangoni convection given in literature [17, 40], the primary bifurcation is axisymmetric to a 3D steady flow. According to [17] and [40] different oscillatory behaviors observed as secondary bifurcation, only when changing the aspect ratio and the Prandtl number. In the present study, all the cases with $Ma_C > 0$, the axisymmetric flow becomes a 3D oscillatory flow as the primary bifurcation when Ma_C increases with a fixed Ma_T for $Ma_T < 2800$. For the cases $Ma_T > 2800$, the flow becomes 3D oscillatory ($m = 3$) as the primary bifurcation when Ma_T increases with a fixed Ma_C.

We start DNSs from the axisymmetric base flow disturbed by the unstable eigenmodes as an initial condition, and, the DNSs converge to stable periodic states as shown in Fig. 4.5. The dominant frequencies are calculated by Fourier spectrum of the time-dependent concentration at a sampling point of $(r, \theta, z) = (0.5A_s^{-1}, 0, 0.5)$. The oscillatory frequencies which are predicted from the imaginary part of the present unstable eigenvalue are in good agreement with those obtained by DNS (Table 4.1).

Figure 4.6 presents the snapshots of DNS results of periodic flow patterns at the middle plane ($z = 0.5$) at (Ma_T, Ma_C) = (0, 1285) and (1750, 928). The non-dimensional time periods (T_p) of the $m = 3$, 4, 5, 6, and 7 are $T_p = 0.56$, 0.37, 0.15, 0.12, and 0.08, respectively. The oscillation frequency is increasing with the azimuthal wavenumber of flow mode at the onset of the convection for $Ma_T = 0 - 2800$.

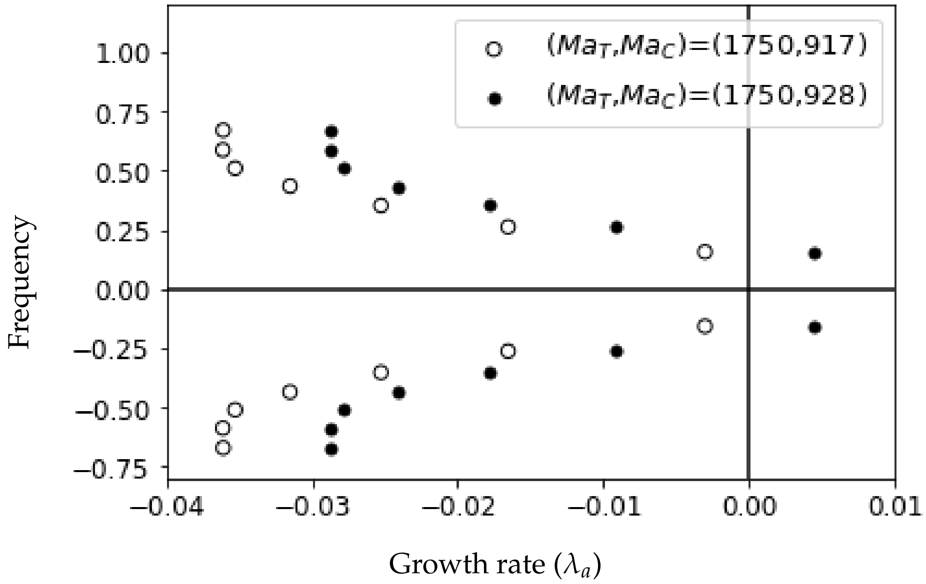

FIGURE 4.2: Eigenvalue spectrum of thermosolutal Marangoni convection onset at $Ma_{\mathrm{T}} = 1750$.

TABLE 4.1: The non-dimensional frequencies of disturbances obtained by DNS and LSA

Ma_{T}	Ma_{C}	DNS	LSA	eigenvalue
0	1285	2.66	2.68	0.0214±0.0945i
700	778	4.15	4.23	0.0235±0.149i
1400	857	5.05	5.00	0.0221±0.1761i
2100	1000	8.02	7.91	0.0151±0.2783i
2800	1220	11.88	11.53	0.0327±0.4059i

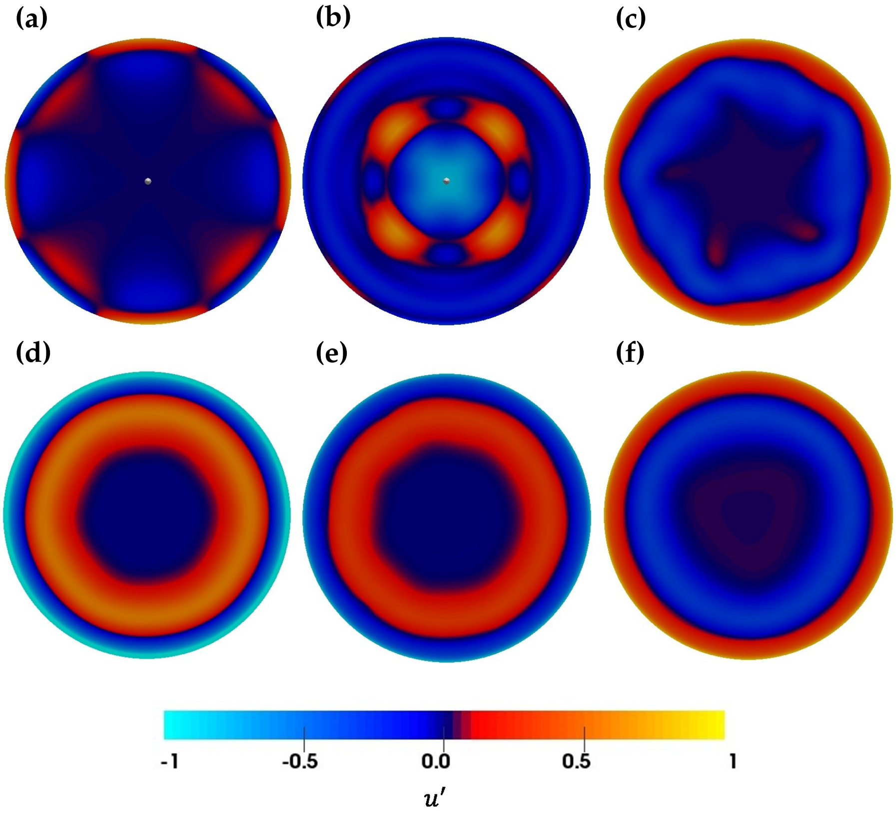

FIGURE 4.3: The vertical velocity, u_z, in the middle plane ($z = 0.5$) of eigenfunctions corresponding to the most unstable eigenmodes: (Ma_{T}, Ma_{C})= (a) (0, 1285), (b) (700, 778), (c) (1750, 928), (d) (2100, 1000), (e) (2800, 1220) and (f) (2926, 500). These cases are also labeled in the stability diagram of Fig. 4.1.

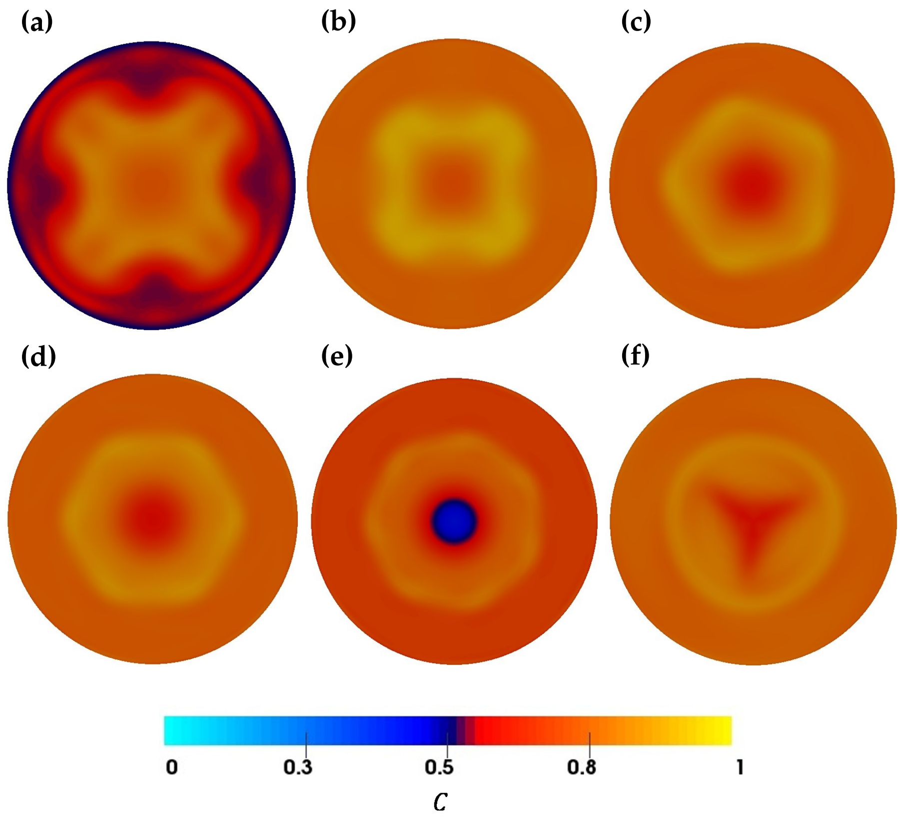

FIGURE 4.4: The nondimensional concentration distributions in the middle plane (at $z = 0.5$) of DNS

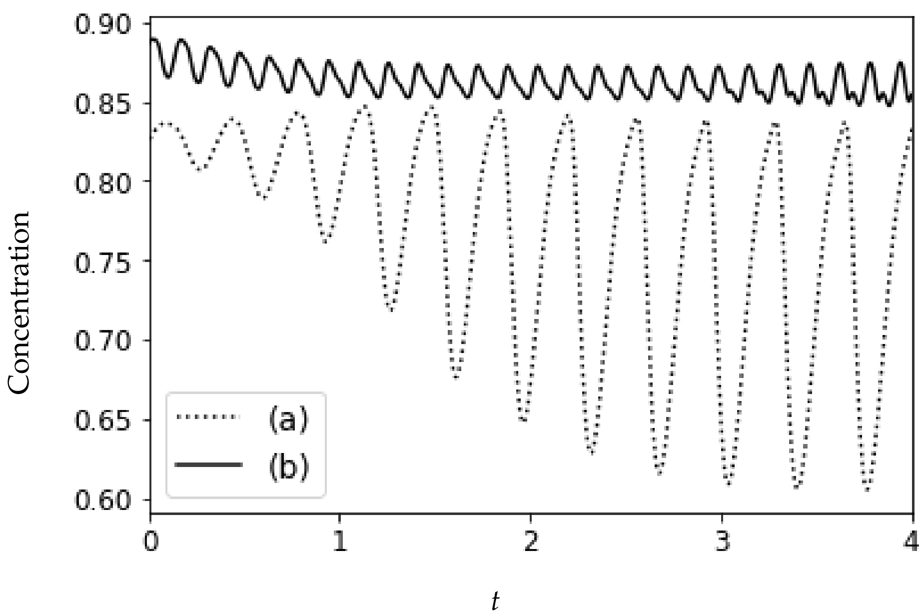

FIGURE 4.5: The time evolution of the nondimensional concentration at the sampling point of $(r, \theta, z) = (0.5A_s^{-1}, 0, 0.5)$ for (Ma_{T}, Ma_{C}) = (a) (0, 1285), (b) (1750, 928). The DNSs are initiated from perturbed axisymmetric base flows.

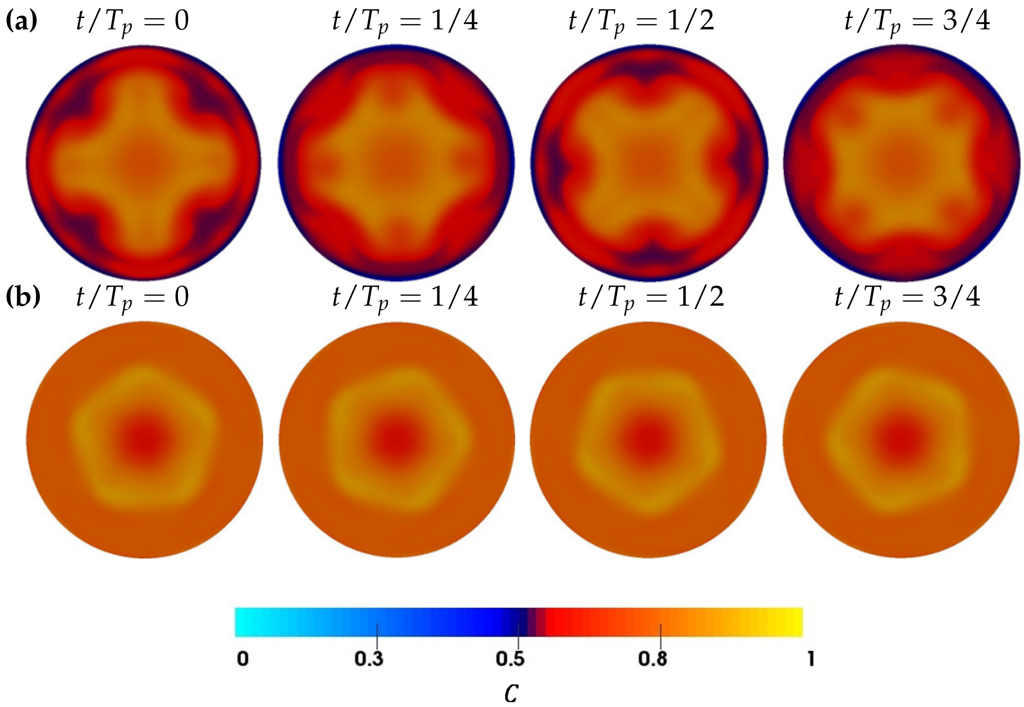

FIGURE 4.6: The time variation of the nondimensional concentration distributions in the middle plane (at $z = 0.5$) of (a) a pulsating periodic flow ($m = 4$) with the period, $T_p = 0.37$, and (b) a travelling wave ($m = 5$) rotating in clockwise with the nondimensional phase speed, $c_\theta = 2\pi/(mT_p)$ where, T_p is 0.15. (a) (Ma_T, Ma_C) = (0, 1285); (b) (1750, 928).

Chapter 5

Onset of thermo-solutal Marangoni convection when the opposite direction of the thermal and solutal Marangoni forces

The onset of thermo-solutal Marangoni convection driven by opposing forces in a half-zone liquid bridge was investigated by the global linear stability analysis.

5.1 Global Stability Analysis

Figure 6.1 shows the stability diagram of the axisymmetric base flow together with previous DNS results (on thermo-solutal Marangoni convection driven by opposing forces) of [78]. Figure 5.2 shows the eigenvalue spectrum at $Ma_{\mathrm{C}} = 357$ near the onset of thermo-solutal Marangoni convection. When the solutal Marangoni number is less than or equal to 360, the imaginary parts of leading eigenvalues (λ with the largest real part) are zero. The leading eigenvalue ($\lambda = 0.00032 \pm 0.0i$) at ($-Ma_{\mathrm{T}}$, Ma_{C})=(470, 357) is indicated with an arrow in Figure 5.2. Figure 5.3 shows the non-dimensional concentration distribution of Si in the middle plane (at $z = 0.5$) of DNS and the least stable eigenmode corresponding to the leading eigenvalue ($\lambda = 0.00032 \pm 0.0i$) at the onset when $Ma_{\mathrm{C}} = 357$. This primary bifurcation implies that a 3D steady flow bifurcates from a 2D axisymmetric pattern when $-Ma_{\mathrm{T}}$ increases. This type of primary bifurcation has been observed commonly in literature for thermal Marangoni convection (see for instance [17, 42]). When $Ma_{\mathrm{C}} > 360$, the bifurcation scenario is different and the least stable eigenmode shows an unstable oscillatory mode. This implies that the 2D axisymmetric flow becomes weakly periodic remaining the flow pattern axisymmetric as Ma_{T} is close to its critical value and eventually flow becomes chaotic at the onset. This result is consistent with the DNS results by [78]. The stability of weakly periodic flow solution is analyzed by applying LSA to a recurring base flow. The real part of the leading eigenvalue of periodic base flow becomes positive at the onset. Figure 5.4 (a) and Figure 5.4 (b) show a detailed example of time snapshots of concentration distribution of Si in the $r-\theta$ plane at $z=0.5$ near the onset when $Ma_{\mathrm{C}}=893$. Figure 5.4 (c) shows the vertical velocity, u_z, in the middle ($z=0.5$) $r-\theta$ plane of eigenfunction corresponding to the most unstable eigenmode when $Ma_{\mathrm{C}}=893$. Figure 5.5 shows the time evaluation of concentration at the sampling point, $(r,\theta,z)=(0.99A_s^{-1},0,0.5)$, near the onset when $Ma_{\mathrm{C}}=893$ and indicates that the flow is weakly periodic and stable before it turns chaotic.

According to the previous study ([45]), when the thermal and solutal Marangoni forces act in the same direction, all the primary bifurcations are from 2D axisymmetric to oscillatory modes. And also, the critical thermal Marangoni numbers ($Ma_{\mathrm{T,Cri}}$) are roughly constant, when $Ma_{\mathrm{C}}\lesssim 800$. According to the present study, $-Ma_{\mathrm{T,Cri}}$ monotonically increases as Ma_{C} increases. The stability line exists slightly below the line of $Ma_{\mathrm{C}}=-Ma_{\mathrm{T}}$ and thus, literally that the flow is steady and 2D axisymmetric when the solutal Marangoni force is dominant. Notably, the flow symmetry breaks, and the flow becomes 3D steady or chaotic when the thermal Marangoni force is dominant. The results imply that the solutal Marangoni convection stabilizes the flow behavior when the thermal and solutal Marangoni forces along the free surface act in opposite directions.

5.2 Bi-stable states of nonlinear equilibria and periodic orbits

To analyze the quasi-periodic flow behavior observed at the onset when $Ma_{\mathrm{C}}>360$, the global LSA was carried out at various $-Ma_{\mathrm{T}}$ values at $Ma_{\mathrm{C}}=893$. Figure 5.6 shows the relative concentration deviation at the sampling point, $(r,\theta,z)=(0.99A_s^{-1},0,0.5)$ across $-Ma_{\mathrm{T}}$ at $Ma_{\mathrm{C}}=893$. In Figure 5.6, the black crosses represent the relative concentration deviation, $(C_{\max}-C_{\min})/C_{\mathrm{avg}}$, calculated by DNS while $-Ma_{\mathrm{T}}$ with the initial condition

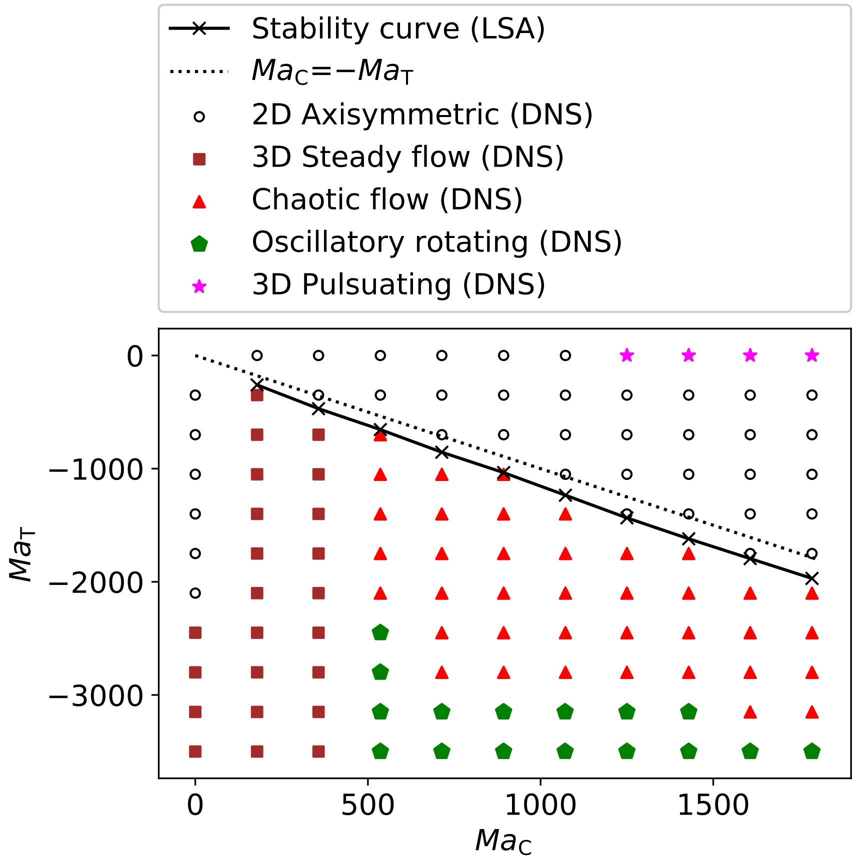

FIGURE 5.1: Stability curve of axisymmetric flow

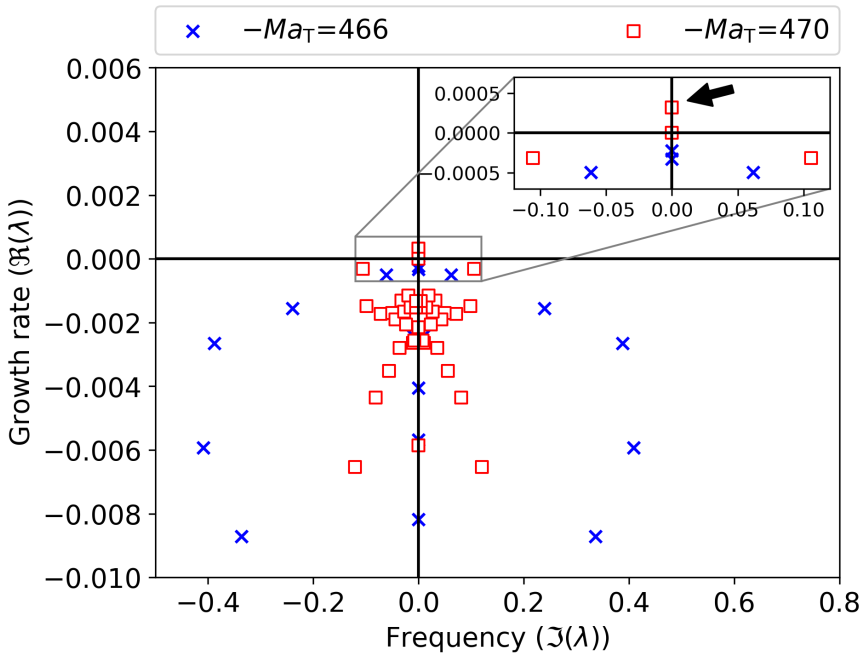

FIGURE 5.2: Eigenvalue spectrum of the onset of thermo-solutal Marangoni convection at $Ma_C = 357$

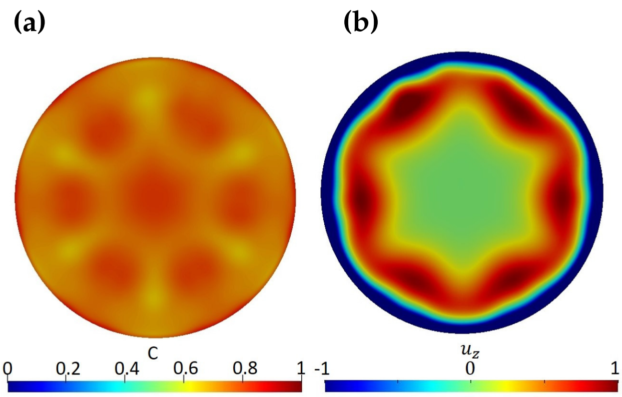

FIGURE 5.3: (a) The non-dimensional concentration distribution of Si in the middle plane (at $z = 0.5$) of DNS at $(-Ma_{\mathrm{T}}, Ma_{\mathrm{C}})$=(470, 357) and (b) The vertical velocity , u_z in the middle ($z = 0.5$) $r - \theta$ plane of eigenfunction corresponding to the most unstable eigenmode at $(-Ma_{\mathrm{T}}, Ma_{\mathrm{C}})$=(470, 357).

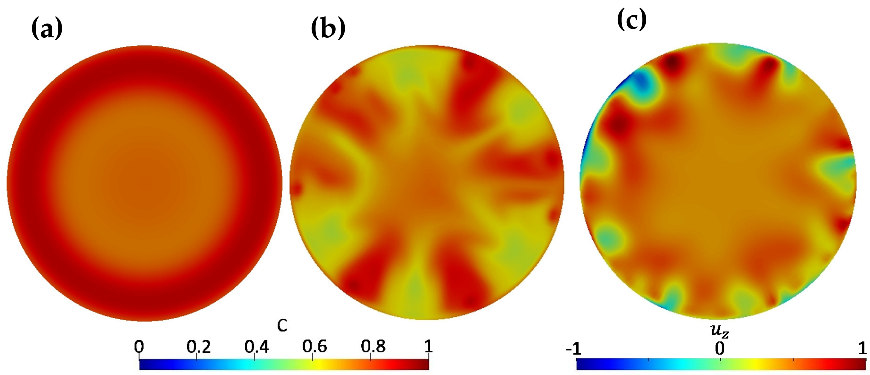

FIGURE 5.4: Non-dimensional concentration distribution of Si in the $r - \theta$ plane at $z = 0.5$: (a) $(-Ma_{\mathrm{T}}, Ma_{\mathrm{C}})$=(1030, 893) and (b) $(-Ma_{\mathrm{T}}, Ma_{\mathrm{C}})$=(1040, 893). (c) - The vertical velocity , u_z in the middle ($z = 0.5$) $r - \theta$ plane of eigenfunction corresponding to the most unstable eigenmode at $(-Ma_{\mathrm{T}}, Ma_{\mathrm{C}})$=(1035, 893).

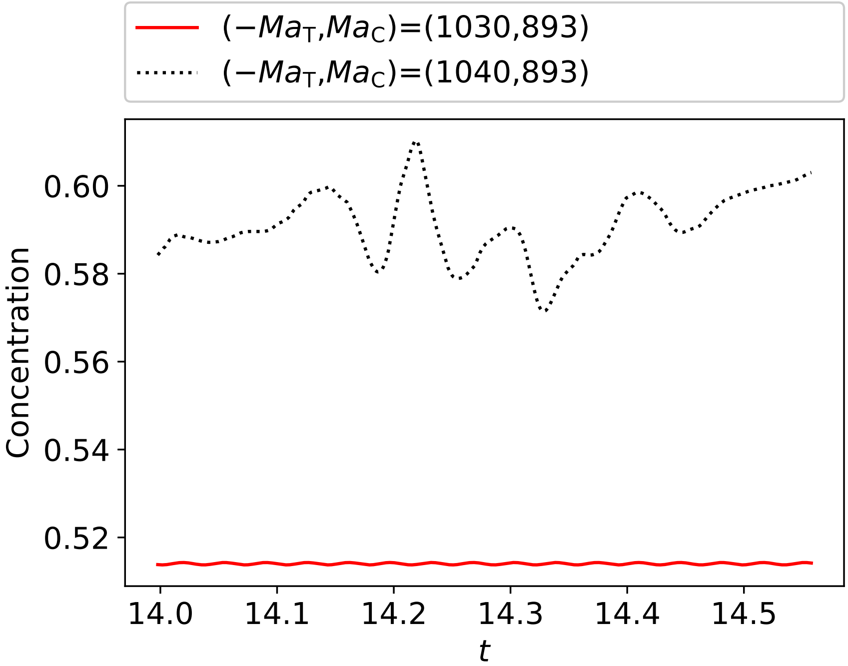

FIGURE 5.5: Time evolution of concentration at the sampling point $(r, \theta, z) = (0.99A_s^{-1}, 0, 0.5)$

being slightly increased (step size in $-Ma_T$ is 1), and the green crosses are also DNS observations but the $-Ma_T$ of the initial conditions are in descending order with decrements of 1 in $-Ma_T$. These DNS results show a hysteresis behavior of the flow field with about 1% difference between the two critical thermal Marangoni numbers. Blue triangles and red squares in Figure 5.6 represent the theoretically predicted steady and periodic flow solutions of the fully-nonlinear governing equations obtained by the Newton-Krylov method. The open and closed symbols represent respectively the unstable and stable solutions. Here "Unstable steady solutions" means the solution is steady with $\Re(\lambda) > 0$ ([102]). Figure 5.7 shows some examples of eigenvalue spectrum of the steady solutions from $-Ma_T = 615$ to 618. The steady solutions at $-Ma_T = 615$ and $-Ma_T = 616$ are stable, where all their eigenvalues have $\Re(\lambda) < 0$. Meanwhile, when $-Ma_T > 616$ all steady state solutions are linearly unstable since the real part of the most unstable eigenvalue with $\Re(\lambda) > 0$ (perturbation grows asymptotically). We also confirmed that the oscillatory time periods which can be predicted from the imaginary part of unstable eigenvalues are in a good agreement with time periods obtained from DNS results as shown in Table 5.1. The stable periodic flow regime appears until $-Ma_T = 1030$ with the increase of $-Ma_T$ and flow losses its stability then becomes a chaotic flow at $-Ma_T = 1040$. This implies that a weak and stable periodic flow regime can be observed when $-Ma_{\mathrm{T}}$ and Ma_{C} are close enough ($-Ma_{\mathrm{T}} \approx Ma_{\mathrm{C}} \pm 200$). As the reason described in [78], the total combined Marangoni flow strength is weakened because of the competing effect of roughly equal thermal and solutal Marangoni flow strengths and also their opposing effects which are responsible for this weak and stable periodic flow regime.

The flow states that keeping the flow behavior exactly the same under some disturbances are known as "invariant solutions", recurrent flows or periodic orbits. Such solutions are important for the understanding of the basic physics behind the flow phenomena we observe since the DNS results depend on the initial conditions. To find the family of periodic solutions across $-Ma_{\mathrm{T}}$ values, the periodic solution at $Ma_{\mathrm{T}} = -619$ was found first. The periodic solution calculated by the Newton-Krylov method at (Ma_{T}, Ma_{C})=$(-619, 893)$ was used as the initial guess in the search of new periodic orbits in neighboring thermal Marangoni numbers, in descending order with $-Ma_{\mathrm{T}} = 1$. When $-Ma_{\mathrm{T}} < 613$, the periodic solutions are unstable and the flow evolves to a steady solution. The Figure 5.8 is visualized the stable periodic solutions from $-Ma_{\mathrm{T}} = 613$ to $-Ma_{\mathrm{T}} = 619$ in the phase plane (time variation of temperature vs time variation of concentration at the sampling point, $(r, \theta, z) = (0.99A_s^{-1}, 0, 0.5)$), where periodic solutions have a characteristic topological signature and their orbits are simple closed curves. The area surrounded by closed curves monotonically increased with $-Ma_{\mathrm{T}}$ as the amplitudes of temperature and concentration at the sampling point, $(r, \theta, z) = (0.99A_s^{-1}, 0, 0.5)$ were increased with $-Ma_{\mathrm{T}}$. As shown in Figure 5.6, when descending in $-Ma_{\mathrm{T}}$ from 619 a stable periodic flow solution was found also at $-Ma_{\mathrm{T}} = 616$. At this particular $-Ma_{\mathrm{T}}$ both steady and periodic solutions are stable and two periodic flow solutions with different amplitudes can be obtained by DNS depending on the initial condition. This observation suggests that the onset of transition from steady to periodic regime is not at the same $-Ma_{\mathrm{T}}$ as the transition is in opposite direction. The results reveal the bi-stability (characteristic of a subcritical Hopf bifurcation) due to the coexistence of two stable flow solutions at the same Marangoni number. When increasing the $-Ma_{\mathrm{T}}$, once the bifurcation point reaches the flow evolve to a stable periodic solution (black crosses corresponding to $-Ma_{\mathrm{T}} = 617$ and 618 in Figure 5.6 are approaching stable periodic solutions when running DNS for a longer time) and when $-Ma_{\mathrm{T}}$ decreased below the lower limit of bi-stability range the flow leads to corresponding stable steady-state solution. The above described two different transitions indicate that the hysteresis phenomena across $-Ma_{\mathrm{T}}$ when thermal and solutal Marangoni convection coexist with opposing forces.

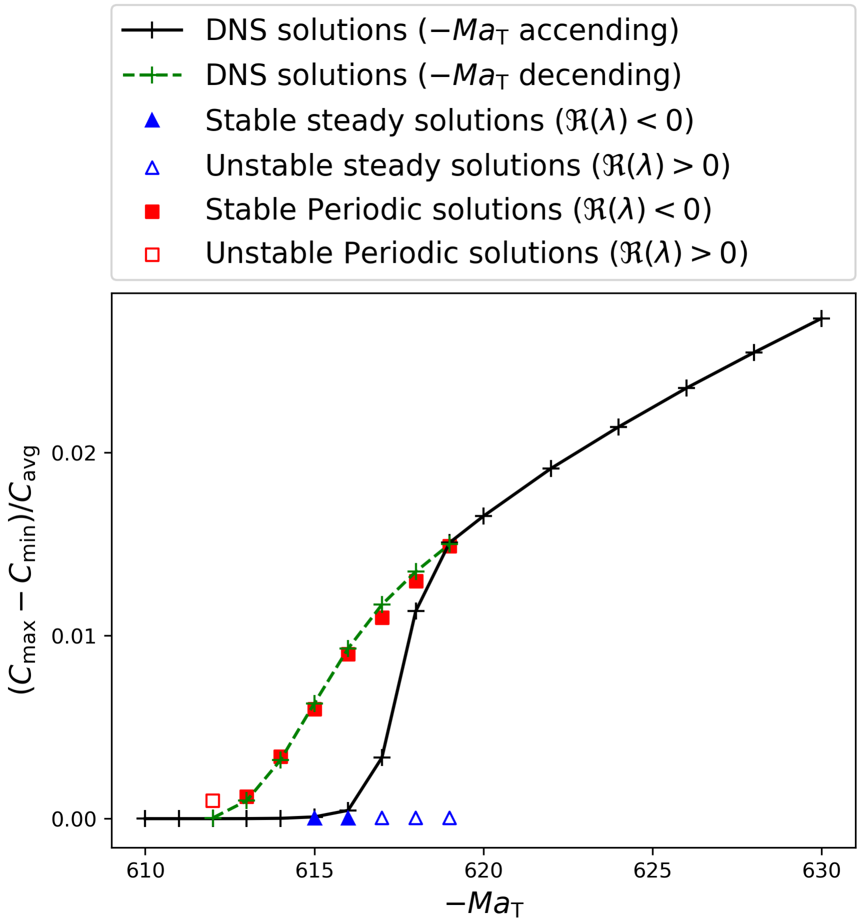

FIGURE 5.6: The relative concentration deviation at the sampling point $((r, \theta, z) = (0.99A_s^{-1}, 0, 0.5))$ across $-Ma_{\mathrm{T}}$ at $Ma_{\mathrm{C}} = 893$.

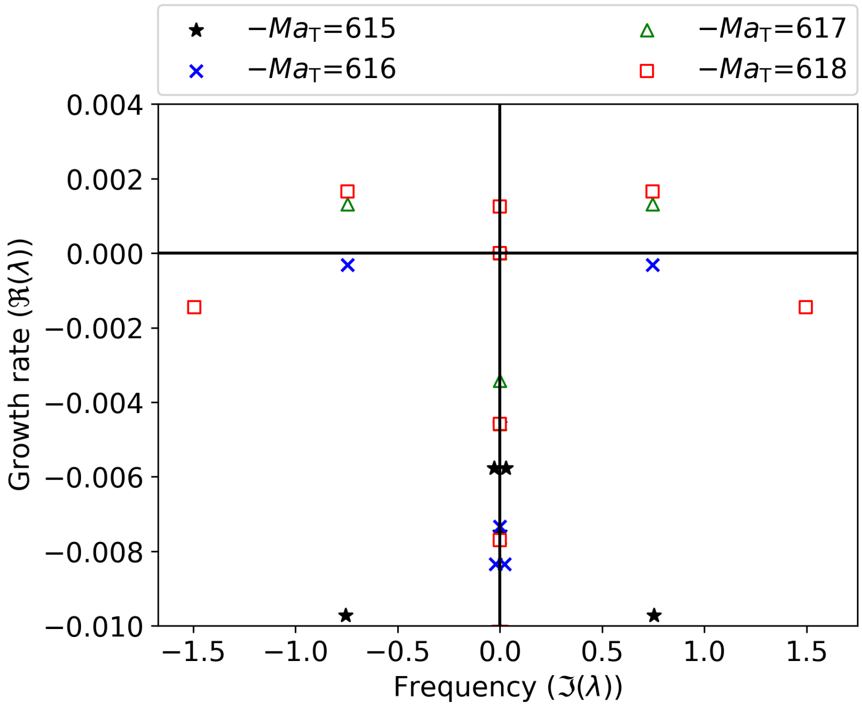

FIGURE 5.7: Eigenvalue spectrum of the family of steady solutions across $-Ma_{\mathrm{T}}$ at $Ma_{\mathrm{C}} = 893$.

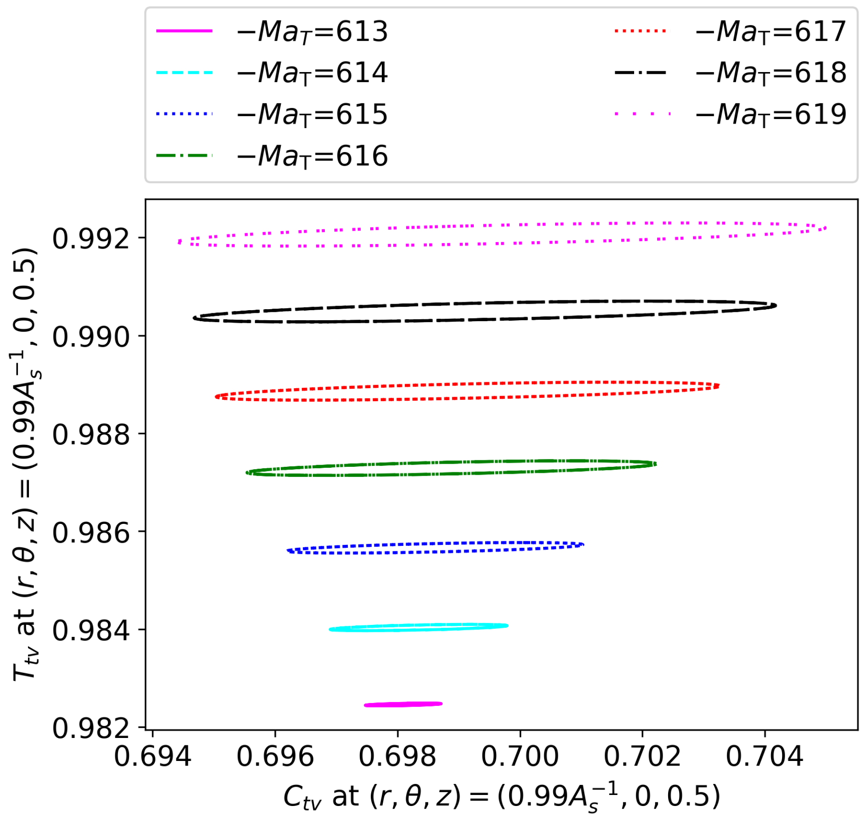

FIGURE 5.8: Phase portraits of the stable periodic solutions from $-Ma_{\mathrm{T}} = 613$ to $-Ma_{\mathrm{T}} = 619$ at $Ma_{\mathrm{C}} = 893$.

TABLE 5.1: The non-dimensional time periods of disturbances obtained by DNS and LSA

$-Ma_\mathrm{T}$	Ma_C	DNS	LSA	eigenvalue
617	893	0.0469	0.047	0.0013±0.7461i
618	893	0.047	0.0471	0.0016±0.7452i

Chapter 6

Flow instabilities in a liquid bridge of smaller aspect ratios

Under this chapter the dependency of flow regimes of thermo-solutal Marangoni convection in the half-zone liquid bridge on aspect ratios (A_s) has been investigated using three-dimensional numerical simulations under zero-gravity.

The flow diagram ($Ma_\mathrm{C}, Ma_\mathrm{T}$) for three different aspect ratios $A_s = 0.25$, $A_s = 0.5$, and $A_s = 1$ are summarized in Figure 6.1, including the previous DNS results of Minakuchi et al. [45] for $A_s = 0.5$. The results indicate that, when Ma_T and Ma_C are sufficiently small, the flow in the liquid bridge is steady and axisymmetric ($m = 0$). When Ma_T as well as Ma_C are larger, the flow becomes 3D oscillatory or 3D steady depending on the aspect ratio of the liquid bridge.

6.1 Critical Ma_C at small thermal Marangoni numbers, $Ma_\mathrm{T} \leq 1800A_s^{-1}$

Present simulations have revealed that, at relatively small $Ma_\mathrm{T} \leq 1800A_s^{-1}$, all the primary bifurcations are from steady axisymmetric flows to 3D rotating oscillatory patterns as shown in the flow maps in Figure 6.1. This direct transition from an axisymmetric steady to a 3D time dependant flow has been reported in many numerical works [28, 29] for high-Pr number fluids. In this study, due to high-Sc number, the primary bifurcation corresponds to the one of high-Pr number fluids. On the other hand, the Marangoni flow of low-Pr number fluids becomes oscillatory via a 3D steady flow when considering pure thermal Marangoni convection [17, 38].

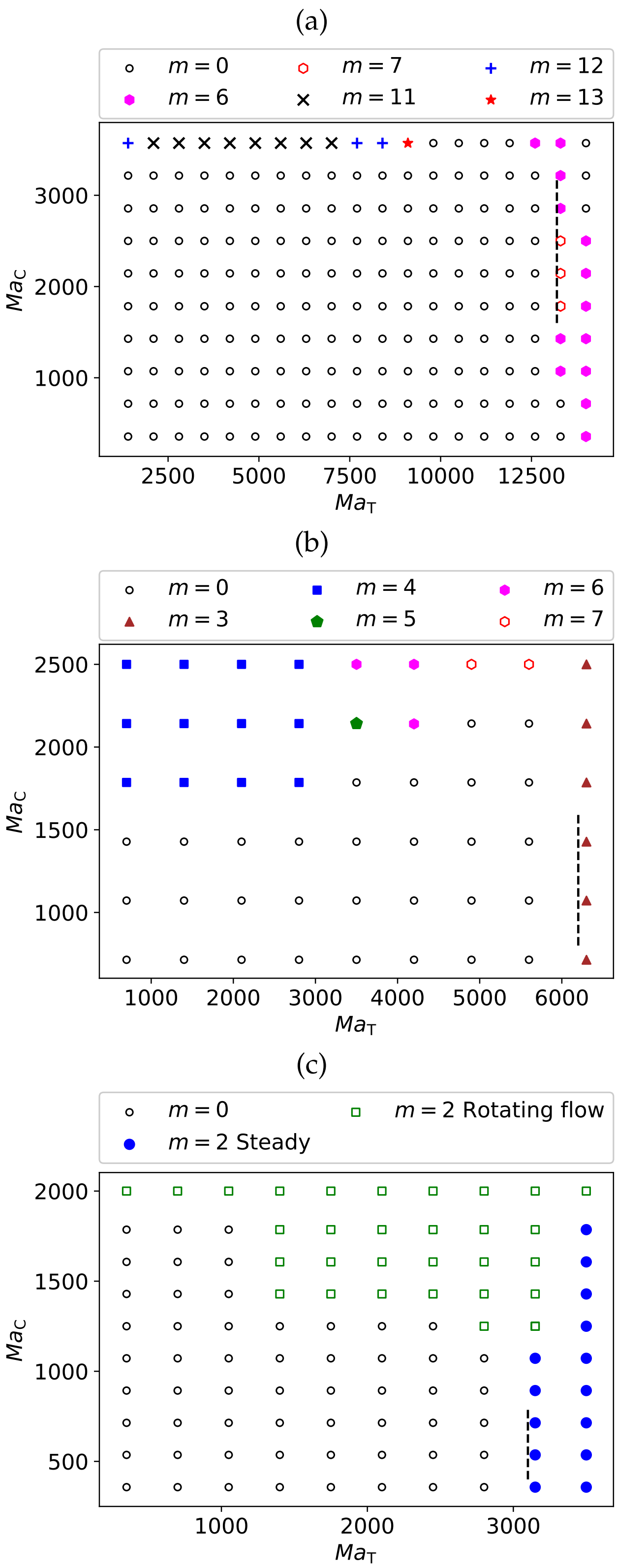

FIGURE 6.1: Flow map, $(Ma_{\mathrm{T}},\ Ma_{\mathrm{C}})$ for (a) $A_s = 0.25$, (b) $A_s = 0.5$ (Minakuchi *et al.* [45]), and (c) $A_s = 1$. The different symbols represent the wavenumbers of oscillatory modes. The dashed lines represent $Ma_{\mathrm{T,Cri}} = 3150A_s^{-1}$ ($400 < Ma_{\mathrm{C}}A_s < 800$), roughly indicating the critical value.

For a shorter liquid bridge, $A_s = 0.25$, when Ma_{C} increases, m-fold symmetric structures for concentration distributions in the middle plane as in Figure 6.2 (a)-(c), and the azimuthal wavenumbers are $m = 11$, 12, and 13 depending on Ma_{T}. The azimuthal wavenumbers $m = 4, 5, 6$, and 7 dependent on Ma_{T} have been reported by Minakuchi et al.[45] at $A_s = 0.5$. Figure 6.3 depicted that the azimuthal wavenumber of oscillatory modes drastically decreases as the aspect ratio increased. The high-frequency wave mode appears, because there is not enough space for the large circulation in the liquid bridge for a flatter aspect ratio. According to Lappa *et al.*[14], in the case of a short liquid zone, Marangoni convection (known as surface phenomena) is confined to a region near the free surface which prevents the coalescence of the opposite convection cell. Thus, several layers of vortices emergence by continuity in the interior of the liquid bridge which leads to the occurrence of the travelling waves with high frequency. A similar dependence of azimuthal wave numbers of oscillatory modes (m) on A_s has been observed in previous studies in the case of pure thermal Marangoni convection [39]. The relationship between m and A_s obtained from the present study is of a roughly constant value, $mA_s = 2.0$–2.75 (Figure 6.3). This range is consistent with those obtained by Chen *et al.* [39] for the $Pr = 0.02$ fluid with $0.4 \leq A_s \leq 2.0$, and is also in good an agreements with those obtained by Wanschura *et al.* [40] especially in the present range, $0.5 \leq A_s \leq 1.3$. It is evident that mA_s becomes nearly constant when the aspect ratios are relatively smaller than $A_s = 1$. The present results also suggest that solutal Marangoni convection does not affect the azimuthal wavenumber of oscillatory modes at small $Ma_{\mathrm{T}} \leq 1800A_s^{-1}$.

In the region, $Ma_{\mathrm{T}} \leq 1800A_s^{-1}$, the critical values, $Ma_{\mathrm{C,Cri}}$, are dependent on the aspect ratio of the liquid bridge. Figure 6.4(a) shows an detailed example at $Ma_{\mathrm{T}} = 0$ and $Ma_{\mathrm{T}} = 1400$. The $Ma_{\mathrm{C,Cri}}$ decreases with A_s, which dependency of $Ma_{\mathrm{C,Cri}}$ on A_s corresponds to the results of pure thermal Marangoni convection for a high-Pr number ($Pr = 1$) fluids [28] shown in Figure 6.4 (b) as dashed line.

According to Chun *et al.* [49], instability mechanism for low-Pr number fluids is not based on the amplification of temperature disturbance because of high thermal diffusivity leads to spread out any possible disturbance over the liquid bridge. In the present study, due to high-Sc number, a concentration disturbance leads to a disturbance of the concentration gradient and thus to a surface tension gradient that triggers a distortion on the velocity field. The distortion of the velocity induces distortion of the concentration field. This coupling

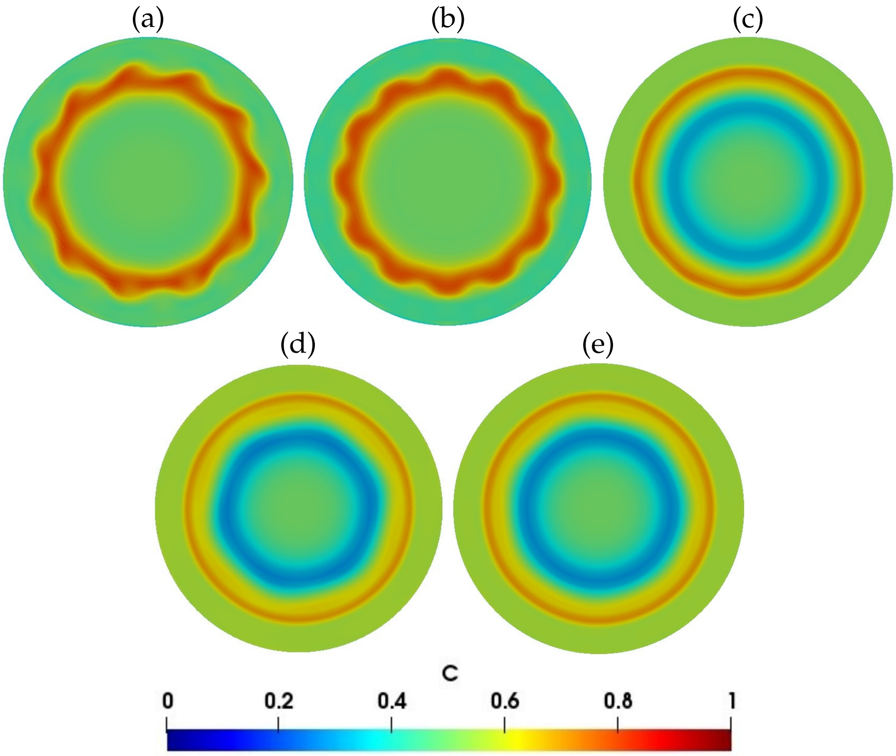

FIGURE 6.2: The non-dimensional concentration distributions in the middle plane ($z = 0.5A_s$) for $A_s = 0.25$ of DNS: ($Ma_{\rm T}$, $Ma_{\rm C}$)= (a) (2100, 3572), (b) (1400, 3572), (c) (9100, 3572), (d) (14000, 1786), and (e) (13300, 1786).

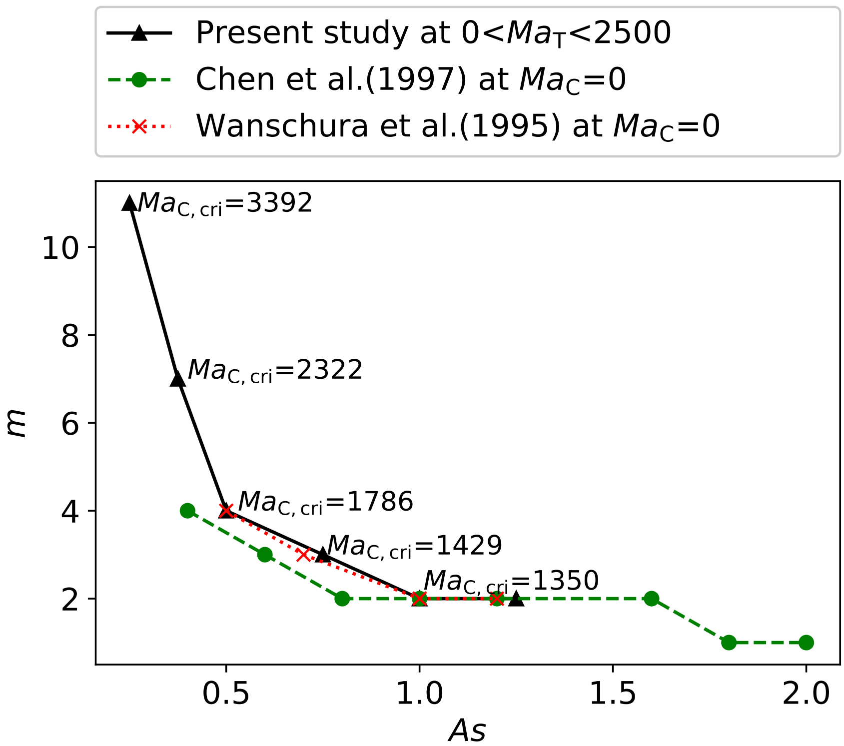

FIGURE 6.3: The azimuthal wavenumbers of the bifurcated oscillatory modes (m) as a function of the aspect ratio of the liquid bridge.

TABLE 6.1: The dominant eigenvalues obtained from DMD and non-dimensional frequencies ((i) at $A_s = 0.25$ and (ii) at $A_s = 1$).

case	A_s	Ma_{T}	Ma_{C}	eigenvalue (λ_1)	frequency	m
(i)	0.25	14000	1786	0.0002±0.1719i	19	6
		13300	1786	0.0002±0.2936i	33	7
		2100	3572	0.0052±0.4877i	55	11
		1400	3572	0.0219±0.4468i	50	12
		9100	3572	0.00006±1.0629i	120	13
(ii)	1	3150	1490	0.006±0.0545i	6.19	2
		3150	1786	0.0032±0.0556i	6.32	2

mechanism is responsible for the growth or decay of the initial concentration disturbance. Thus, the instability mechanism emerged as hydrosolutal in nature.

The frequency spectrum of the time-dependant concentration at a sampling point of $(r, \theta, z) = (0.75, 0, 0.5A_s)$ when (Ma_{T}, Ma_{C})= (9100, 3572) in Figure 6.5 shows that the azimuthal travelling waves are associated with harmonics of their fundamental frequencies. The dynamic mode decomposition results are used to determine fundamental frequencies of azimuthal travelling waves developed in the liquid bridge. Representative dynamic modes for $A_s = 0.25$ are displayed in Figure 6.6 using the concentration field in the middle plane ($z = 0.5A_s$); their respective eigenvalues and calculated frequencies are given in Case (i) of Table 6.1. The calculated time periods from DMD for $A_s = 0.25$ show good agreements with the time periods of the concentration at the sampling point of $(r, \theta, z) = (0.75, 0, 0.5A_s)$ as show in Figure 6.7.

6.2 Critical Ma_{T} under a weak solutal Marangoni convection

When $Ma_{\mathrm{C}} \leq 700A_s^{-1}$ as Ma_{T} increases, the axisymmetric steady flow becomes 3D oscillatory for shorter liquid bridges ($A_s = 0.25$ and 0.5). We note thst the flow transition for a long liquid bridge ($A_s = 1$) is from axisymmetric steady (Figure 6.8 (a)) to 3D steady (Figure 6.8 (b)). The critical thermal Marangoni number $Ma_{\mathrm{T,Cri}}$ decreases with the aspect ratio of the liquid bridge and a similar trend can be observed for the results of pure thermal Marangoni convection by Imaishi *et al.*[17] as shown in Figure 6.4 (b). Under the presence of weak solutal Marangoni convection, the critical thermal Marangoni number is roughly $Ma_{\mathrm{T,Cri}}A_s \approx 3200$ at the small solutal Marangoni numbers, $400 \lesssim Ma_{\mathrm{C}}A_s \lesssim 800$, as shown by the dashed lines in Figure 6.1(a-c).

(a)

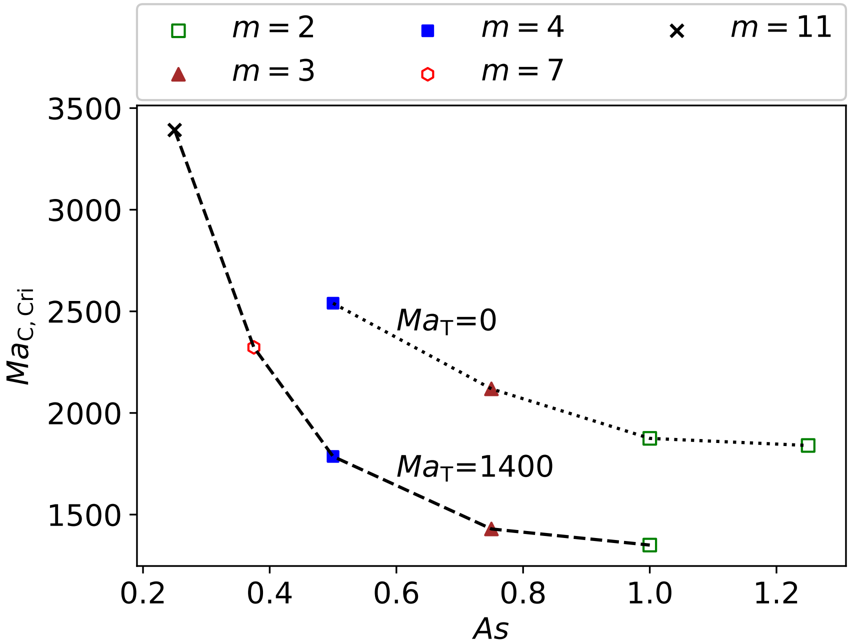

(b)

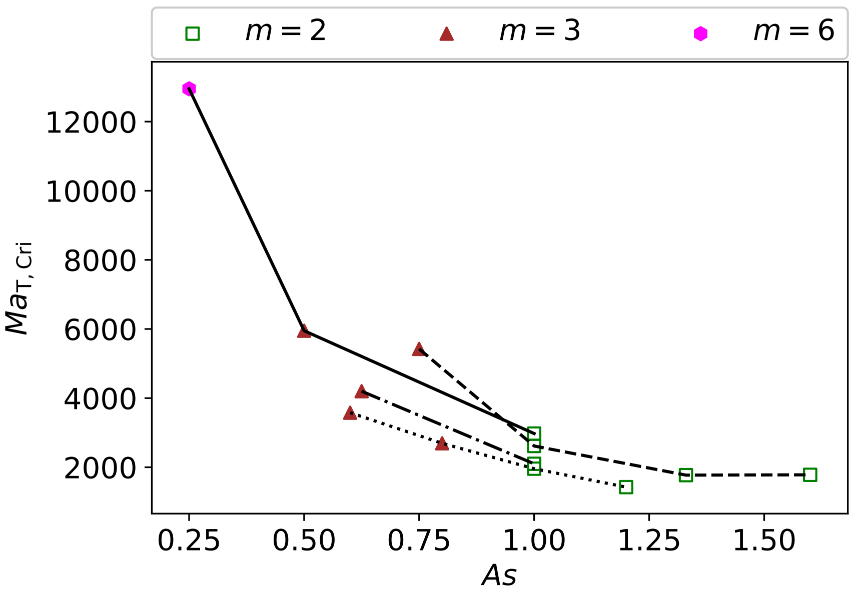

FIGURE 6.4: (a) Dependency of critical solutal Marangoni numbers, $Ma_{\mathrm{C,Cri}}$, on the aspect ratio of the liquid bridge. The lines are the stability curves: $Ma_{\mathrm{T}} = 0$ and $Ma_{\mathrm{T}} = 1400$. (b) Critical thermal Marangoni number $Ma_{\mathrm{T,Cri}}$ as a function of A_s: ——, Present (at $Ma_{\mathrm{C}} = 714$ and $Pr = 0.006$); —·—, Present (at $Ma_{\mathrm{C}} = 0$ and $Pr = 0.006$); ······, Imaishi *et al.* [17] ($Ma_{\mathrm{C}} = 0$, $Pr = 0$); −−−−, Yasuhiro *et al.* [28] ($Ma_{\mathrm{C}} = 0$, $Pr = 1$). The different symbols represent the wavenumbers of oscillatory modes.

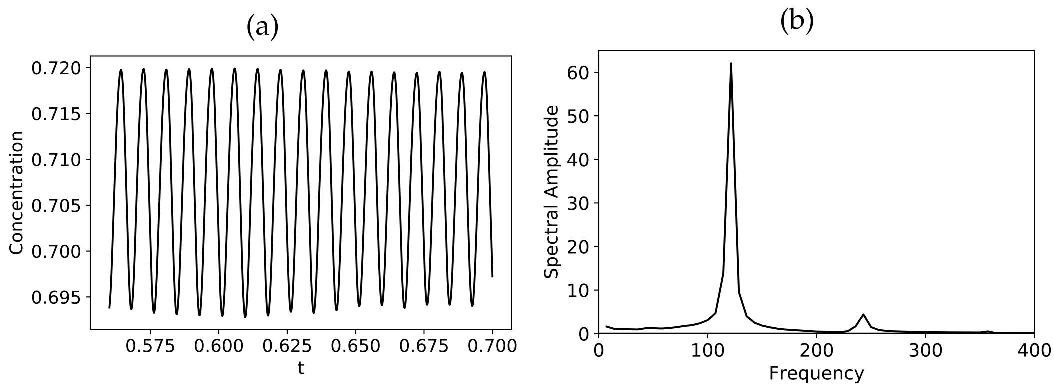

FIGURE 6.5: The time evolution of the non-dimensional concentration for $A_s = 0.25$ at the sampling point of $(r, \theta, z) = (0.75, 0, 0.5A_s)$ when $(Ma_\mathrm{T}, Ma_\mathrm{C}) = (9100, 3572)$ (a) and the frequency spectrum (b).

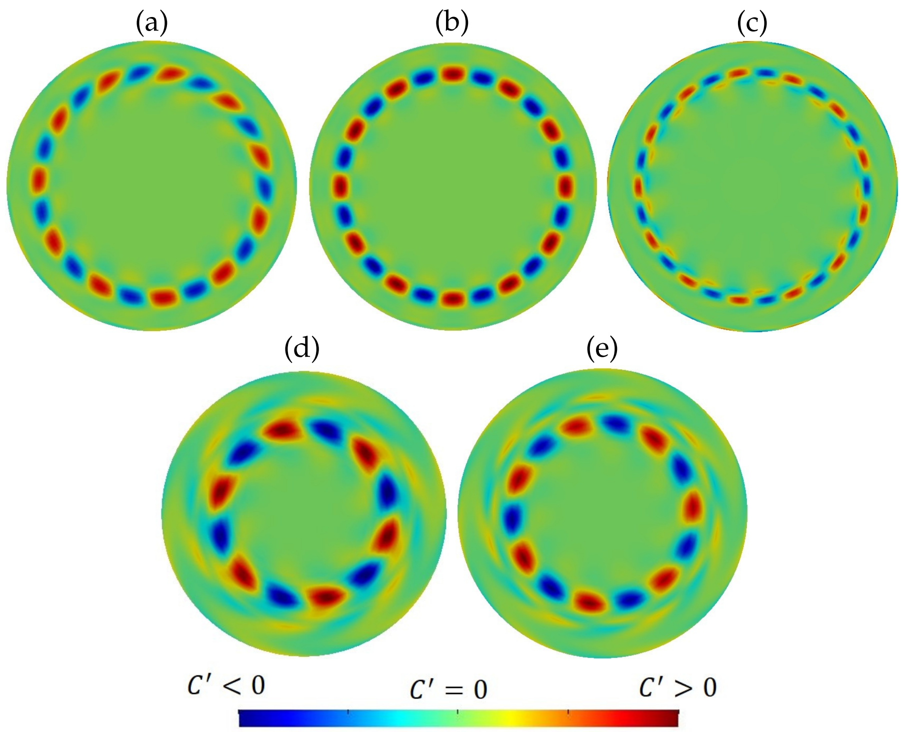

FIGURE 6.6: Representative dynamic modes corresponding to the primary dominant eigenvalues, visualized by contours of the concentration field in the middle plane ($z = 0.5A_s$) for a flat liquid bridge, $A_s = 0.25$: (Ma_T, Ma_C)= (a) (2100, 3572), (b) (1400, 3572), (c) (9100, 3572), (d) (14000, 1786), and (e) (13300, 1786).

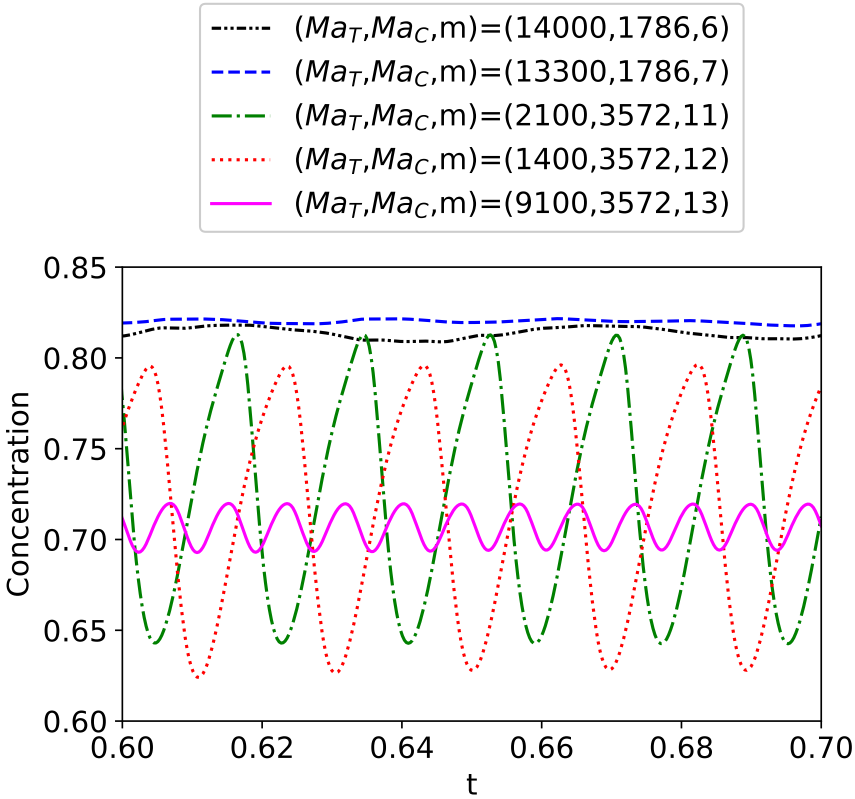

FIGURE 6.7: The time evolution of the non-dimensional concentration for $A_s = 0.25$ at the sampling point of $(r, \theta, z) = (0.75, 0, 0.5A_s)$.

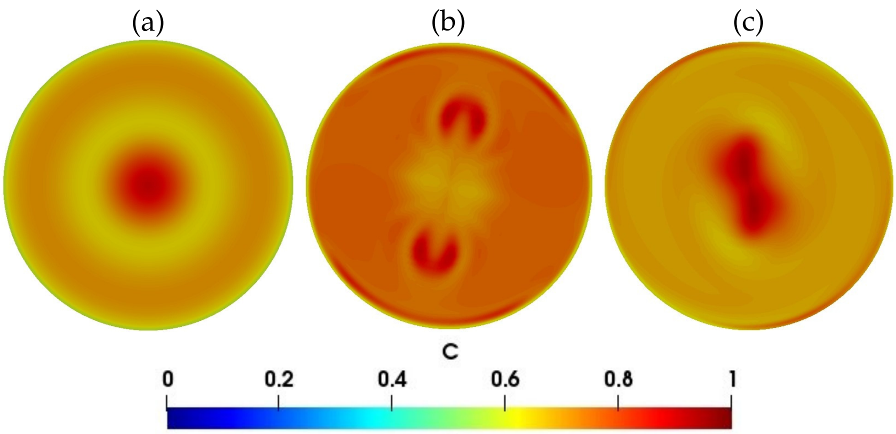

FIGURE 6.8: The non-dimensional concentration distributions in the middle plane (at $z = 0.5A_s$ and $A_s = 1$) of DNS:(Ma_{T}, Ma_{C})= (a) (1050, 1786), (b) (3500, 1786), and (c) (3150,1786).

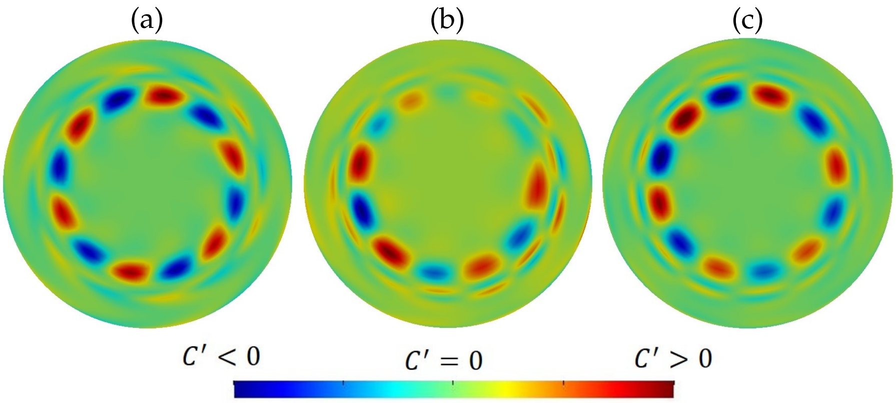

FIGURE 6.9: Representative dynamic modes corresponding to the second leading eigenvalues, visualized by contours of the concentration field in the middle plane (at $z = 0.5A_s$ and $A_s = 0.25$): (Ma_{T}, Ma_{C}, λ_2)= (a) (13300, 1784, 0.00005$\pm$0.2764i), (b) (13300, 2144, -0.0029$\pm$0.3518i), and (c) (13300, 2500, -0.0006$\pm$0.3351i).

The higher azimuthal wave numbers ($m = 6$ in Figure 6.2(d) and $m = 7$ in Figure 6.2(e)) are observed for a short liquid bridge ($A_s = 0.25$) as Ma_{T} increases due to the limited space inside the liquid bridge, hence the characteristic length for $A_s \lesssim 1$ is the height of the liquid bridge L.

Figure 6.2 shows that the flow patterns with $m = 6$ and 7 do not distinctly appear compared to $m = 11$ and 12. This observation is confirmed by Figure 6.7 as the concentration values corresponding to $m = 11$ and 12 are relatively higher than those corresponding to $m = 6$ and 7. Figure 6.9 shows the representative dynamic modes ($m = 6$) corresponding to second leading eigenvalues (λ_2) for (Ma_{T}, Ma_{C})= (13300, 1786), (13300, 2144), and (13300, 2500) at $A_s = 0.25$. For these three cases dynamic modes corresponding to dominant eigenvalues (λ_1) are shown $m = 7$ (see Figure 6.6(e)). It is concluded that the azimuthal traveling waves of $m = 6$ (passively) and $m = 7$ are superimposed when (Ma_{T}, Ma_{C})= (13300, 1786), (13300, 2144), and (13300, 2500).

For $A_s = 1$, when $Ma_{\mathrm{C}} \geq 1250$ as Ma_{T} increases, after a certain threshold, the steady axisymmetric flow departs to rotating oscillatory flow with $m = 2$ (Figure 6.8 (c)), and eventually, the flow becomes 3D steady (Figure 6.8 (b)) while the azimuthal wavenumber remains unchanged if Ma_{T} further increases. The extracted spatio-temporal coherent structures (Figure 6.10) and respective frequencies (case(ii) of Table 6.1) of traveling waves associated with rotating oscillatory flow regime are computed by DMD. The non-dimensional concentration

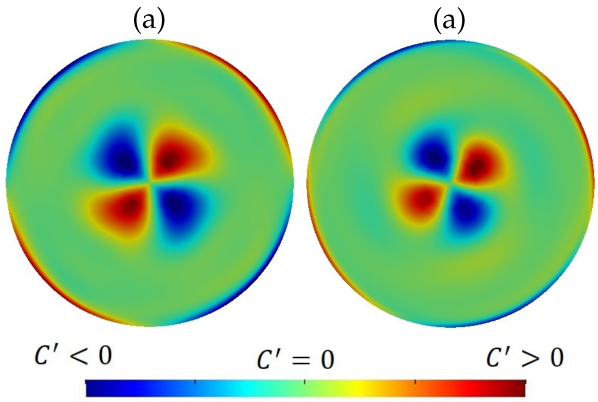

FIGURE 6.10: The non-dimensional concentration distributions in the middle plane at $z = 0.5A_s$ obtained DMD analysis for $A_s = 1$: (Ma_{T}, Ma_{C})= (a) (3150, 1490) and (b) (3150, 1786).

with respect time calculated by DNS for (Ma_{T}, Ma_{C}) = (3150, 1490) and (1350, 1786) in rotating oscillatory flow regime at the sampling point of $(r, \theta, z) = (0.5, 0, 0.5A_s)$ and $A_s = 1$ is presented in Figure 6.11. The frequencies of traveling waves are close each other when (Ma_{T}, Ma_{C}) = (3150, 1490) and (3150, 1786) even though Ma_{C} increased.

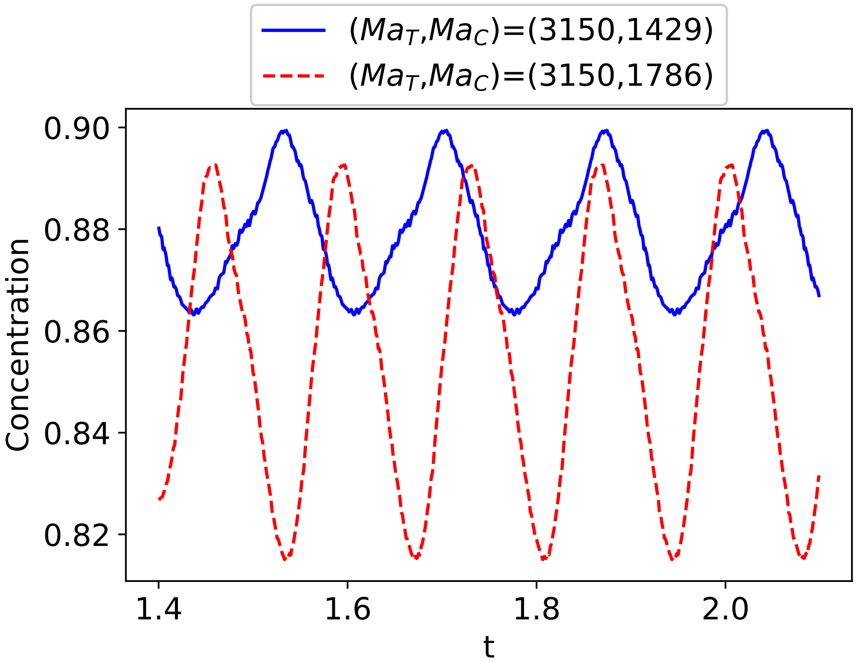

FIGURE 6.11: The time variation of the non-dimensional concentration for $A_s = 1$ at the sampling point of $(r, \theta, z) = (0.5, 0, 0.5A_s)$.

Chapter 7

Conclusions

A new method for the exact prediction of instability of thermo-solutal Marangoni convection in a half-zone liquid bridge under zero gravity was successfully developed. The global LSA was performed to determine the critical thermal and critical solutal Marangoni numbers. Stability limits are highly dependent on both the solutal and thermal Marangoni numbers even at the constant aspect ratio and Prandtl number values. The steady axisymmetric flows become oscillatory flows (Hopf bifurcations) with azimuthal wave-numbers $m = 3$, 4, 5, 6, and 7 at the onset for the range of thermal and solutal Marangoni numbers considered in the present study. For pure thermal Marangoni convection in literature, the primary bifurcation is 2D axisymmetric to a 3D steady flow. On the other hand, the primary bifurcation in this study was 2D axisymmetric to a 3D oscillatory flow at the onset as increasing the thermal Marangoni number. The stability range of the present global LSA is consistent with the previous DNS results on thermo-solutal Marangoni convection.

The onset of thermo-solutal Marangoni convection driven by opposing forces in a half-zone liquid bridge was investigated by the global LSA. The stability curve exists slightly below the line of $Ma_{\mathrm{C}} = -Ma_{\mathrm{T}}$ confirming that the flow is 2D axisymmetric when the solutal Marangoni force is dominant. A family of steady flow solutions along with a family of periodic flow solutions across various $-Ma_{\mathrm{T}}$ values were calculated by the Newton-Krylov method for the first time at the onset of thermo-solutal Marangoni convection driven by opposing forces. The eigenvalues instability was evaluated across $-Ma_{\mathrm{T}}$ values to investigate the bifurcation point. The onset of transition from steady to a periodic flow and that of its reverse transition do not occur at the same Marangoni number, which reveals the subcritical Hopf bifurcation of steady and periodic flow regimes. This indicates that the stable steady and periodic flow solutions may coexist over a short Ma_T range. Thus, the results were confirmed hysteresis phenomena across thermal Marangoni numbers when thermal and solutal Marangoni convection coexists with opposing forces.

The computed stability limits presented in this study would be useful to avoid possible flow-induced disturbances and lead to the growth of single crystals without growth striations, in FZ experiments under normal and microgravity gravity conditions.

The dependency of flow regimes of thermo-solutal Marangoni convection in the half-zone liquid bridge on aspect ratios (A_s) has been investigated using three-dimensional numerical simulations under zero-gravity. The dependency of $Ma_\mathrm{C,cri}$ on A_s for weak solutal Marangoni convection is in good agreement with the previous results of the case of pure thermal Marangoni convection for high-Pr number fluids. $Ma_\mathrm{T,Cri}$ values are decreased as A_s increases, which is similar to the previous results for the case of pure thermal Marangoni convection. From our results, for a short liquid bridge ($A_s \leq 1$), the critical $Ma_\mathrm{T,Cri}A_s$ in the case of a weak solutal Marangoni convection is roughly constant 3200. The Marangoni convection is limited by the height of the liquid bridge which determines the characteristic length of the Marangoni convection that becomes comparable to the radius with increasing A_s (the flow behaviour changes at $A_s \approx 1$), consistent with the previous analysis of the pure thermal Marangoni convection in tall liquid bridges with $A_s \gtrsim 1$. The flow pattern in the flat liquid bridge is analyzed by DMD. The azimuthal wavenumbers of oscillatory modes are increased when the aspect ratio of the liquid bridge gets smaller. From results of present study, $mA_s \approx 2.0$–2.75 is obtained, which is a similar relationship obtained in previous studies in the case of pure thermal Marangoni convection. The azimuthal wavenumbers of oscillatory modes are insusceptible of solutal Marangoni convection. The results suggest that the selection of the characteristic length of the Marangoni convection depends on A_s of the liquid bridge.

7.1 Future works

This thesis demonstrated the instability mechanisms behind the thermo-solutal Marangoni convection in the half-zone liquid bridge under zero-gravity conditions. This study can be further investigated with the following aspects.

1. The present work is done by considering the half-zone model of the floating zone method under zero gravity. Under normal gravity, the natural convection applies together with Marangoni convection and the flow behavior becomes more complex than zero gravity conditions. It is important to study flow instabilities under normal gravity conditions by considering free surface deformation of the liquid bridge as the geometry is not perfectly cylindrical under normal gravity conditions.

2. The investigation of the relative contribution of the aspect ratio of the liquid bridge on the convection onset of half zone liquid bridge under normal gravity conditions is also important to be studied in the future.

3. In the real floating zone system, the heating coils are placed outside the melt, moving together with the growing crystal and providing the temperature distribution to the free surface. Given this situation, the electromagnetic field generated by the heating coil directly affects the main flow. The effect of electromagnetic field by heating coil on the instability of thermo-solutal Marangoni convection can be further investigated in the future.

Appendix A

Introduction to finite volume method

In numerical mathematics, partial differential equations are solved by first converting them to a corresponding set of algebraic equations. This is done by a method called discretization. There are a number of discretization techniques available such as finite volume method, finite element method, finite difference method, spectral element method, boundary element method and high-resolution discretization schemes. In the present study, the equations are discretized by finite volume method using the built in libraries of the CFD tool OpenFOAM. Finite volume discretization process can be divided into three main steps [103],

- Discretization of time
- Discretization of space
- Discretization of Equations

A.1 Discretization of time

Time is discretized by separating the time domain over which the solution is required into a set of time steps Δt, which may change during the simulation. During the solution procedure, time is marched from a prescribed initial condition.

A.2 Discretization of space

Discretization of space is achieved by sub dividing the solution geometry into a number of cells called control volumes. These cells should not overlap with one another and should fill the computational domain. The centroids of these cells determine the points of space at

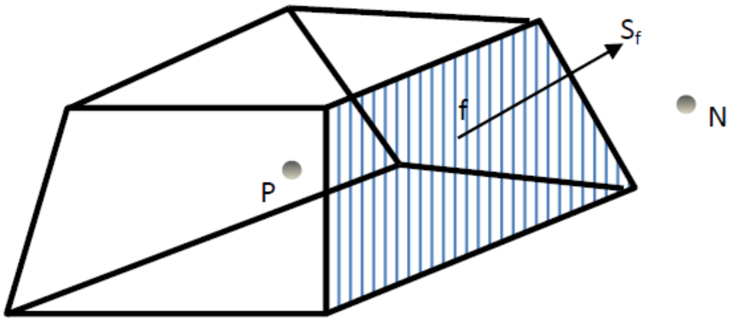

FIGURE A.1: A typical control volume in finite volume method

which the solution is required. A typical control volume and its associated properties are presented in Figure A.1. The control volume is bounded by flat faces, represented by letter f. Cell faces belong to two main categories, internal faces and boundary faces. Internal faces are the faces between two control volumes and boundary faces coincide with boundaries of the solution domain. Each face of internal cells is shared with only one neighbour cell. Properties are usually defined at cell centroids, P. The face area vector, S_f is of magnitude equal to the area of the face and points outwards from the control volume perpendicular to the face [103].

A.3 Discretization of equations

The general form of the conservation equation for a scalar property can be written as,

$$\frac{\partial \phi}{\partial t} + div\,(\rho \phi u) - div\,(\tau grad \phi) = S_{\phi} \tag{A.1}$$

The finite volume method requires that this equation should be satisfied in integral form over the control volume around the point at which the solution is sought [103]. This requires:

$$\int_{t}^{t+\Delta t} \left[\frac{\partial}{\partial t} \int \rho \phi dV + \int \bigtriangledown \cdot (\rho \Gamma \bigtriangledown \phi)\, dV \right] dt = \int_{t}^{t+\Delta t} \left(\int S_{\phi dV} \right) dt \tag{A.2}$$

A.3.1 Spatial discretization

The first spatial term of equation (A.2) is discretized as,

$$\int \rho\phi dV = \rho\phi_p V_p \tag{A.3}$$

The volume integrals of the above equation are converted into surface integrals over control volume surface using the following identities of vector calculus;

$$\int \bigtriangledown \cdot A dV = \int A \cdot dS \int \bigtriangledown \cdot \phi dV = \int \phi \cdot dS \tag{A.4}$$

This results in following relationship for convective and diffusive terms of the general conservation equation,

$$\int \bigtriangledown \cdot (\rho U \phi)\, dV = \int (\rho U \phi) \cdot dS \tag{A.5}$$

Since the control volume is bounded by a series of flat faces, the surface integral on the right-hand side can be written as a sum of integrals over separate faces. Therefore

$$\int (\rho U \phi)\, dV = \Sigma_f \int (\rho U \phi) \cdot dS \tag{A.6}$$

The face integral is evaluated using face value of ϕ and ρU and is given by

$$\int (\rho U \phi)\, dS = (\rho U)_f \cdot S_f \phi_f \tag{A.7}$$

This provides the discretized form of the convective term as,

$$\int \bigtriangledown \cdot (\rho U \phi)\, dV = \Sigma_f\, (\rho U)_f \cdot S_f \phi_f \tag{A.8}$$

Using the above procedure, the laplacian term is discretized as,

$$\int \bigtriangledown \cdot (\rho\Gamma \bigtriangledown \phi)\, dV = \int (\rho\Gamma \bigtriangledown \phi)\, dS \int \bigtriangledown \cdot (\rho\Gamma \bigtriangledown \phi)\, dV = \Sigma_f \int (\rho\Gamma \bigtriangledown \phi)\, dS \tag{A.9}$$

Therefore,

$$\int \bigtriangledown \cdot (\rho\Gamma \bigtriangledown \phi)\, dV = \Sigma_f \rho\Gamma \left(\bigtriangledown\phi\right)_f \cdot S_f \tag{A.10}$$

The discretized form of integral terms can be evaluated using face values and face centre values of neighbour cells. The entire set of discretized equations written over the solution domain represents a system of simultaneous linear equations. This linear set of equations is solved during each iteration of solution algorithm using numerical procedures for linear systems.

Appendix B

Arnoldi method

The Jacobian $\boldsymbol{A}$ is $N \times N$ real matrix, here N is the number of freedom of a flow state x and the freedom is $N \approx O(10^6)$. To overcome to obtain the eigenvalues of the huge size of $\boldsymbol{A}$, we use the Arnoldi method to find some largest eigenvalues and corresponding eigenvectors approximately from a reduced matrix in Krylove subspace. The features of the Arnoldi method are,
(i) We do not need to store $\boldsymbol{A}$ on memory in the machine.
(ii) Arnoldi methods approximate the larger eigenvalues accurately
(iii) The algorithm of the Arnoldi process requires matrix-vector products, $\boldsymbol{Ax}$ which is computed by using a DNS code.

Let the krylov subspace $K_s = span(\delta x, \boldsymbol{A}\delta x, \boldsymbol{A}^2\delta x, ..., \boldsymbol{A}^n\delta x)(n \ll N)$ is spanned by orthonormal set $\boldsymbol{q}_k(k = 1, ..., n)$, then the algorithm of Arnoldi process is

$x_1 = initial\ vector\ (arbitrary)$
$\boldsymbol{q}_1 = x_1/\sqrt{(x_1 \cdot x_1)}$
$Perform\ until\ convergence\ (k = 1, ..., n)$
$x_{k+1} = \boldsymbol{A}\boldsymbol{q}_k - \sum_{j=1}^{k} h_{j,k}\boldsymbol{q}_k$
$h_{j,k} = (\boldsymbol{q}_j \cdot \boldsymbol{A}\boldsymbol{q}_k)$
$h_{k+1,k} = \sqrt{(x_{k+1} \cdot x_{k+1})}$
$\boldsymbol{q}_{k+1} = x_{k+1}/h_{k+1,k}$

here $\boldsymbol{H} = h_{j,k}$ is a Hessengerg matrix. Some least unstable eigenvalues of $\boldsymbol{A}$ are approximately shared with those of $\boldsymbol{H}$. Matrix-vector product $\boldsymbol{A}\boldsymbol{q}_k$ is given by
$\mathbf{Aq}_k \approx \frac{\int_0^{\tau}(f(x+\varepsilon\mathbf{q}_k)-f(x))dt}{\varepsilon}$

Which is performed by using DNS code, because $f(x)$ is obtained by calculation of the time integration of right hand side of Navier-Stokes equation from the initial condition x. Note that $|\mathbf{q}_k| = 1$ and $|\varepsilon|$ should be small to be in the linear regime ($|\varepsilon| \sim O(10^{-6})$, practically).

Bibliography

[1] M. Yildiz, S. Dost, and B. Lent. "Growth of bulk SiGe single crystals by liquid phase diffusion". In: *J. Cryst. Growth* **280** (2005), pp. 151–160. DOI: 10.1016/j.jcrysgro.2005.03.030.

[2] M. Yildiz, S. Dost, and B. Lent. "Evolution of the growth interface in liquid phase diffusion growth of bulk SiGe single crystals". In: *Cryst. Res. Technol.* **41** (2006), pp. 211–216. DOI: 10.1002/crat.200510561.

[3] S. Dost and Brian Lent. *Dost and Lent: Single Crystal Growth of Semiconductors from Metallic Solutions*. Elsevier B.V, Jan. 2007. ISBN: 978-0-444-52232-0.

[4] D. Schwabe and A. Scharmann. "Marangoni convection in open boat and crucible". In: *J. Cryst. Growth* **52** (1981), pp. 435–449. DOI: 10.1016/0022-0248(81)90231-1.

[5] Y. J. Kim and Sindo Kou. "Thermocapillary convection in zone-melting crystal growth - An open-boat physical simulation". In: *J. Cryst. Growth* **98** (1989), pp. 637–645. DOI: 10.1016/0022-0248(89)90300-X.

[6] J. R. Ristorcelli and J. L. Lumley. "Instabilities, transition and turbulence in the Czochralski crystal melt". In: *J. Cryst. Growth* **116** (1992), pp. 447–460. DOI: 10.1016/0022-0248(92)90654-2.

[7] Shin Nakamura et al. "Thermal waves of a nonaxisymmetric flow in a Czochralski-type silicon melt". In: *J. Cryst. Growth* **207** (1999), pp. 55–61. DOI: 10.1016/S0022-0248(99)00357-7.

[8] Marcello Lappa, ed. *Fluids, Materials and Microgravity - 1st Edition*. First. Elsevier, 2004, p. 538.

[9] T A Campbell et al. "Float zone growth and characterization of $Ge_1 - x\ Si_x$ ($x < 10$ at%) single crystals". In: *J. Cryst. Growth* **226** (2001), pp. 231–239.

[10] Yasutomo Arai et al. “Study of SiGe Crystal Growth Interface Processed in Microgravity”. In: *Cryst. Growth Des.* **18** (2018), pp. 3697–3703. DOI: 10.1021/acs.cgd.8b00544.

[11] A Croll et al. “Floating-Zone Growth of GaAs under Microgravity during the D2-Mission”. In: *Cryst. Res. Technol* **29** (1994). DOI: 10.1002/crat.2170290308.

[12] A. Eyer and H. Leiste. “Striation-free silicon crystals by float-zoning with surface-coated melt”. In: *J. Cryst. Growth* **71** (1985), pp. 249–252. DOI: 10.1016/0022-0248(85)90073-9.

[13] Suguru Shiratori, Hendrik C. Kuhlmann, and Taketoshi Hibiya. “Linear stability of thermocapillary flow in partially confined half-zones”. In: *Phys. Fluids* **19** (2007), p. 44103. DOI: 10.1063/1.2714021.

[14] M. Lappa. “Three-dimensional numerical simulation of Marangoni flow instabilities in floating zones laterally heated by an equatorial ring”. In: *Phys. Fluids* **15** (2003), pp. 776–789. DOI: 10.1063/1.1543147.

[15] Marcello Lappa. “CHAPTER 1 - Space research”. In: *Fluids, Materials and Microgravity*. Ed. by Marcello Lappa. Oxford: Elsevier, 2004, pp. 1 –37. DOI: 10.1016/B978-008044508-3/50002-5.

[16] Y. Masuda et al. “Numerical simulation of heat transfer in floating zone single crystal growth process with radio-frequency induction heating”. In: *Int. J Heat Mass Transfer* **39** (1996), pp. 3035–3043. DOI: 10.1016/0017-9310(95)00377-0.

[17] N. Imaishi et al. “Numerical simulation of oscillatory Marangoni flow in half-zone liquid bridge of low Prandtl number fluid”. In: *J. Cryst. Growth* **230** (2001), pp. 164–171. DOI: 10.1016/S0022-0248(01)01332-X.

[18] Toru Ogasawara et al. “Secondary instability induced by thermocapillary effect in half-zone liquid bridge of high Prandtl number fluid”. In: *Mech. Eng. Lett.* **5** (2019), pp. 19–00014. DOI: 10.1299/mel.19-00014.

[19] C. W. Lan and J. H. Chian. “Three-dimensional simulation of Marangoni flow and interfaces in floating-zone silicon crystal growth”. In: **230** (2001), pp. 172–180. DOI: 10.1016/S0022-0248(01)01328-8.

[20] P. Dold, A. Gröll, and K. W. Benz. "Floating-zone growth of silicon in magnetic fields I. Weak static axial fields". In: *J. Cryst. Growth* **183** (1998), pp. 545–553. DOI: 10.1016/S0022-0248(97)00485-5.

[21] You-Rong Li et al. "Three-dimensional oscillatory thermocapillary flow in encapsulated liquid bridge". In: *Phys. Fluids* **18** (2006), p. 074108. DOI: 10.1063/1.2227051.

[22] Z Zeng et al. "Direct numerical simulation of oscillatory Marangoni convection in cylindrical liquid bridges". In: *J. Cryst. Growth* **204** (1999), pp. 395–404. DOI: 10.1016/S0022-0248(99)00207-9.

[23] Hisashi Minakuchi, Yasunori Okano, and Sadik Dost. "A three-dimensional numerical simulation study of the Marangoni convection occurring in the crystal growth of Si_xGe_{1-x} by the float-zone technique in zero gravity". In: *J. Cryst. Growth* **266** (2004), pp. 140–144. DOI: 10.1016/j.jcrysgro.2004.02.038.

[24] H Minakuchi, Y Okano, and S Dost. "The Hysteresis Phenomena of Flow Patterns due to Thermal and Solutal Marangoni Convections in a Liquid Bridge under Zero Gravity". In: *Fluid Mech. Res. Int. J.* **2** (2018), p. 00018. DOI: 10.15406/fmrij.2018.02.00018.

[25] Th Kaiser and K W Benz. " Floating-zone growth of silicon in magnetic fields III. Numerical simulation". In: *J. Cryst. Growth* **183** (1998), pp. 564–572.

[26] L. Carotenuto et al. "Instability of thermocapillary convection in liquid bridges". In: *Phys. Fluids* **10** (1998), pp. 555–565. DOI: 10.1063/1.869583.

[27] M Lappa and R Savino. *International journal for numerical methods in fluids parallel solution of three-dimensional Marangoni flow in liquid bridges*. Tech. rep. 1999, pp. 911–935. DOI: 10.1002/(SICI)1097-0363(19991130)31:6.

[28] S Yasuhiro et al. "Numerical simulation of three-dimensional oscillatory thermocapillary flow in a half zone of Pr=l fluid". In: *Adv. Space. Res* **24** (1999), pp. 1385–1390.

[29] Jens Leypoldt, Hendrik C. Kuhlmann, and Hans J. Rath. "Three-dimensional numerical simulation of thermocapillary flows in cylindrical liquid bridges". In: *J. Fluid Mech.* **414** (2000), pp. 285–314. DOI: 10.1017/S0022112000008570.

[30] Mårten Levenstam, Gustav Amberg, and Christian Winkler. "Instabilities of thermocapillary convection in a half-zone at intermediate Prandtl numbers". In: *Phys. Fluids* **13** (2001), pp. 807–816. DOI: 10.1063/1.1337063.

[31] R. Savino and R. Monti. "Oscillatory Marangoni convection in cylindrical liquid bridges". In: *Phys. Fluids* **8** (1996), pp. 2906–2922. DOI: 10.1063/1.869070.

[32] Shouichi Yasuhiro, Tsuneyuki Sato, and Nobuyuki Imaishi. *Three-Dimensional Oscillatory Marangoni Flow in Half-Zone Liquid Bridges of Pr=1 Fluid*. Tech. rep. Kyushu University, 2000, pp. 321–326.

[33] P. Dold et al. "Floating zone growth of silicon in magnetic fields:: IV. Rotating magnetic fields". In: *J. Cryst. Growth* **231** (2001), pp. 95–106. DOI: 10.1016/S0022-0248(01)01491-9.

[34] Y. Kamotani, S. Ostrach, and M. Vargas. "Oscillatory thermocapillary convection in a simulated floating-zone configuration". In: *J. Cryst. Growth* **66** (1984), pp. 83–90. DOI: 10.1016/0022-0248(84)90079-4.

[35] Dietrich Schwabe. "Thermocapillary liquid bridges and Marangoni convection under microgravity - Results and lessons learned". In: *Microgravity Sci. Technol.* **26** (2014), pp. 1–10. DOI: 10.1007/s12217-014-9358-0.

[36] Yong Zou et al. "Effect of Rotating Magnetic Field on Thermal Convection and Dopant Transport in Floating-Zone Crystal Growth". In: *Microgravity Sci. Technol.* **32** (2020), pp. 349–361. DOI: 10.1007/s12217-019-09776-w.

[37] Rodolfo Monti. "On the onset of the oscillatory regimes in Marangoni flows". In: *Acta Astronaut.* **15** (1987), pp. 557–560. DOI: 10.1016/0094-5765(87)90156-1.

[38] R Rupp, G Müller, and G Neumann. "Three-dimensional time dependent modelling of the Marangoni convection in zone melting configurations for GaAs". In: *J. Cryst. Growth* **97** (1989), pp. 34–41. DOI: 10.1016/0022-0248(89)90244-3.

[39] G. Chen, A. Lizée, and B. Roux. "Bifurcation Analysis of the thermocapillary convection in cylindrical Liquid Bridges". In: *J. Cryst. Growth* **180** (1997), pp. 638–647. DOI: 10.1016/S0022-0248(97)00259-5.

[40] M. Wanschura et al. "Convective instability mechanisms in thermocapillary liquid bridges". In: *Phys. Fluids* **7** (1995), pp. 912–925. DOI: 10.1063/1.868567.

[41] C. H. Chun and W. Wuest. "Experiments on the transition from the steady to the oscillatory Marangoni-convection of a floating zone under reduced gravity effect". In: *Acta Astronaut.* **6** (1979), pp. 1073–1082. DOI: 10.1016/0094-5765(79)90056-0.

[42] K. Motegi, K. Fujimura, and I. Ueno. "Floquet analysis of spatially periodic thermocapillary convection in a low-Prandtl-number liquid bridge". In: *Phys. Fluids* **29** (2017), p. 074104. DOI: 10.1063/1.4993466.

[43] H. Minakuchi, Y. Okano, and S. Dost. "Effect of thermo-solutal Marangoni convection on the azimuthal wave number in a liquid bridge". In: *J. Cryst. Growth* **468** (2017), pp. 502–505. DOI: 10.1016/j.jcrysgro.2016.09.028.

[44] Yasunori Okano, Ako Hatano, and Akira Hirata. "Natural and Marangoni Convections in a Floating Zone". In: *J. Chem. Eng. Japan* **22** (1989), pp. 385–388. DOI: 10.1252/jcej.22.385.

[45] Hisashi Minakuchi, Tatsuya Yoshino, and Ysunori Okano. "The relative contributions and control of thermo-solutal Marangoni convections on flow patterns in a liquid bridge (in Japanese)". In: *Proc. of The 63rd Nat. Cong. of Theoretical & Applied Mechanics* (2014), pp. 055–25. DOI: 10.1016/j.jcrysgro.2013.05.042.

[46] I. Martinez and A. Eyer. "Liquid bridge analysis of silicon crystal growth experiments under microgravity". In: *J. Cryst. Growth* **75** (1986), pp. 535–544. DOI: 10.1016/0022-0248(86)90099-0.

[47] Dieter Langbein. "Crystal growth from liquid columns". In: *J. Cryst. Growth* **104** (1990), pp. 47–59. DOI: 10.1016/0022-0248(90)90307-7.

[48] D. Schwabe and A. Scharmann. "Thermocapillary convection in crystal growth melts". In: *Lett. heat mass transf.* **7** (1980), pp. 283–292. DOI: 10.1016/0094-4548(80)90013-2.

[49] Ch H. Chun. "Experiments on steady and oscillatory temperature distribution in a floating zone due to the Marangoni convection". In: *Acta Astronaut.* **7** (1980), pp. 479–488. DOI: 10.1016/0094-5765(80)90037-5.

[50] D. Schwabe, R. Velten, and A. Scharmann. "The instability of surface tension driven flow in models for floating zones under normal and reduced gravity". In: *J. Cryst. Growth* **99** (1990), pp. 1258–1264. DOI: 10.1016/S0022-0248(08)80117-0.

[51] G Chen and Bernard Roux. *An analytical study of thermocapillary flow and surface deformations in floating zone*. Tech. rep. 1991, pp. 73–80.

[52] A. Rybicki and J. M. Floryan. “Thermocapillary effects in liquid bridges. I. Thermocapillary convection”. In: *Phys. Fluids* **30** (1987), p. 1956. DOI: `10.1063/1.866210`.

[53] Yiqiang Zhang and J. Iwan D. Alexander. “Surface tension and buoyancy-driven flow in a non-isothermal liquid bridge”. In: *Int. J. Numer. Methods Fluids* **14** (1992), pp. 197–215. DOI: `10.1002/fld.1650140207`.

[54] C. W. Lan and Sindo Kou. “Thermocapillary flow and melt/solid interfaces in floating-zone crystal growth under microgravity”. In: *J. Cryst. Growth* **102** (1990), pp. 1043–1058. DOI: `10.1016/0022-0248(90)90873-J`.

[55] J. C. Chen, C. F. Chu, and W. F. Ueng. “Thermocapillary convection and melt-solid interface in the floating zone”. In: *Int. J. Heat Mass Transf.* **37** (1994), pp. 1733–1748. DOI: `10.1016/0017-9310(94)90063-9`.

[56] J. C. Chen and C. F. Chu. “Numerical computation of fluid flow of floating-zone crystal growth of molybdenum”. In: *Int. J. Heat Mass Transf.* **38** (1995), pp. 1841–1853. DOI: `10.1016/0017-9310(94)00305-F`.

[57] Jyh Chen Chen and Hsian Kun Wu. “Numerical computation of heat flow, fluid flow and interface shapes in the float zone of lithium niobate during a melting process”. In: *Int. J. Heat Mass Transf.* **39** (1996), pp. 3707–3716. DOI: `10.1016/0017-9310(96)00003-8`.

[58] E. Chénier, C. Delcarte, and G. Labrosse. “Stability of the axisymmetric buoyant-capillary flows in a laterally heated liquid bridge”. In: *Phys. Fluids* **11** (1999), pp. 527–541. DOI: `10.1063/1.869927`.

[59] J. C. Chen and G. H. Chin. “Linear stability analysis of thermocapillary convection in the floating zone”. In: *J. Cryst. Growth* **154** (1995), pp. 98–107. DOI: `10.1016/0022-0248(95)00095-X`.

[60] G. Kasperski, A. Batoul, and G. Labrosse. “Up to the unsteadiness of axisymmetric thermocapillary flows in a laterally heated liquid bridge”. In: *Phys. Fluids* **12** (2000), pp. 103–119. DOI: `10.1063/1.870286`.

[61] A. Cröll et al. “Floating-zone and floating-solution-zone growth of GaSb under microgravity”. In: *J. Cryst. Growth* **191** (1998), pp. 365–376. DOI: 10.1016/S0022-0248(98)00215-2.

[62] Mårten Levenstam et al. “Experimental and numerical studies of thermocapillary convection in a floating zone like configuration”. In: *J. Cryst. Growth* **158** (1996), pp. 224–230. DOI: 10.1016/0022-0248(95)00466-1.

[63] M. Lappa and R. Savino. “3D analysis of crystal/melt interface shape and Marangoni flow instability in solidifying liquid bridges”. In: *J. Comput. Phys.* **180** (2002), pp. 751–774. DOI: 10.1006/jcph.2002.7131.

[64] J. J. Xu and S. H. Davis. “Convective thermocapillary instabilities in liquid bridges”. In: *Phys. Fluids* **27** (1984), pp. 1102–1107. DOI: 10.1063/1.864756.

[65] R. Velten, D. Schwabe, and A. Scharmann. “The periodic instability of thermocapillary convection in cylindrical liquid bridges”. In: *Phys. Fluids A* **3** (1991), pp. 267–279. DOI: 10.1063/1.858135.

[66] Dong Ming Mo and Deng Fang Ruan. “Linear-Stability Analysis of Thermocapillary-Buoyancy Convection in an Annular Two-Layer System with Upper Rigid Wall Subjected to a Radial Temperature Gradient”. In: *Microgravity Sci. Technol.* **31** (2019), pp. 293–304. DOI: 10.1007/s12217-019-9692-3.

[67] W E Arnoldi. “The Principle of Minimized Iterations in The Solution of The Matrix Eigenvalue Problem”. In: *Q Appl Math.* **9** (1951), pp. 17–29. DOI: doi.org/10.1090/qam/42792.

[68] Vassilis Theofilis. “Global Linear Instability”. In: *Ann. Rev. Fluid Mech.* **43** (2011), pp. 319–352. DOI: 10.1146/annurev-fluid-122109-160705.

[69] Y. Saad. “Variations on Arnoldi’s method for computing eigenelements of large unsymmetric matrices”. In: *Linear Algebra Its Appl.* **34** (1980), pp. 269–295. DOI: 10.1016/0024-3795(80)90169-X.

[70] F. Gómez, R. Gómez, and V. Theofilis. “On three-dimensional global linear instability analysis of flows with standard aerodynamics codes”. In: *Aerospace Sci. Technol.* **32** (2014), pp. 223–234. DOI: 10.1016/j.ast.2013.10.006.

[71] Peter J. Schmid. "Dynamic mode decomposition of numerical and experimental data". In: *J. Fluid Mech.* **656** (2010), pp. 5–28. DOI: 10.1017/S0022112010001217.

[72] Clarence W. Rowley et al. "Spectral analysis of nonlinear flows". In: *J. Fluid Mech.* **641** (2009), pp. 115–127. DOI: 10.1017/S0022112009992059.

[73] Mihailo R. Jovanović, Peter J. Schmid, and Joseph W. Nichols. "Sparsity-promoting dynamic mode decomposition". In: *Phys. Fluids* **26** (2014), p. 24103. DOI: 10.1063/1.4863670.

[74] Matthew O. Williams, Ioannis G. Kevrekidis, and Clarence W. Rowley. "A Data–Driven Approximation of the Koopman Operator: Extending Dynamic Mode Decomposition". In: *J. Nonlinear Sci.* **25** (2015), pp. 1307–1346. DOI: 10.1007/s00332-015-9258-5.

[75] Steven L. Brunton, Joshua L. Proctor, and J. Nathan Kutz. "Sparse Identification of Nonlinear Dynamics with Control (SINDYc)". In: *IFAC-PapersOnLine* **49** (2016), pp. 710–715. DOI: 10.1016/j.ifacol.2016.10.249.

[76] Yann T. Delorme et al. "Dynamic mode decomposition of Fontan hemodynamics in an idealized total cavopulmonary connection". In: *Fluid Dyn. Res.* **46** (2014). DOI: 10.1088/0169-5983/46/4/041425.

[77] Erik Berger et al. "Estimation of perturbations in robotic behavior using dynamic mode decomposition". In: *Adv Robot .* **29** (2015), pp. 331–343. DOI: 10.1080/01691864.2014.981292.

[78] Chihao Jin et al. "Characterization of the thermal and solutal Marangoni flows of opposite directions developing in a cylindrical liquid bridge under zero gravity". In: *Phys. Fluids* **32** (2020), p. 034104. ISSN: 1070-6631. DOI: 10.1063/1.5142071.

[79] Genta Kawahara, Markus Uhlmann, and Lennaert Van Veen. "The Annual Review of Fluid Mechanics is online at". In: *Annu. Rev. Fluid Mech* **44** (2012), pp. 203–225. DOI: 10.1146/annurev-fluid-120710-101228.

[80] M. Lappa, R. Savino, and R. Monti. "Three-dimensional numerical simulation of Marangoni instabilities in liquid bridges: Influence of geometrical aspect ratio". In: *Int. J. Numer. Methods Fluids* **36** (2001), pp. 53–90. DOI: 10.1002/fld.120.

[81] F Preisser, D Schwabe, and A Scharmann. “Steady and oscillatory thermocapillary convection in liquid columns with free cylindrical surface”. In: *J. Fluid Mech* **126** (1983), pp. 545–567. DOI: 10.1017/s0022112083000324.

[82] Chengcheng Le, L. Liu, and Zaoyang Li. “Numerical investigation of the effect of rotation on the oscillatory thermocapillary convection and dopant transport in a silicon liquid bridge”. In: *J. Cryst. Growth* **523** (2019). DOI: 10.1016/j.jcrysgro.2019.125149.

[83] Hisashi Minakuchi et al. “A grid refinement study of half-zone configuration of the Floating Zone growth system”. In: *J. Adv. Res. Phys.* **3** (2012), p. 011201.

[84] S Abbasoglu and I Sezai. “Three-dimensional modelling of melt flow and segregation during Czochralski growth of Ge_xSi_{1-x} single crystals”. In: *Int. J. Thermal Sci.* **46** (2007), pp. 561–572.

[85] Hendrik C. Kuhlmann. “Introduction”. In: *Thermocapillary Convection in Models of Crystal Growth*. Springer Berlin Heidelberg, 2007. DOI: 10.1007/bfb0109563.

[86] Ò Liu Qiong et al. “Instability and sensitivity analysis of flows using OpenFOAMÂ®”. In: *Chinese J. Aeronaut.* **29** (2016), pp. 316–325. DOI: 10.1016/j.cja.2016.02.012.

[87] Uwe Ehrenstein. “On the linear stability of channel flow over riblets”. In: *Phys. Fluids* **8** (1996), pp. 3194–3196. DOI: 10.1063/1.869091.

[88] Ramesh Natarajan. “An Arnoldi-based iterative scheme for nonsymmetric matrix pencils arising in finite element stability problems”. In: *J. Comput. Phys.* **100** (1992), pp. 128–142. DOI: 10.1016/0021-9991(92)90315-P.

[89] Ramesh Natarajan and Andreas Acrivos. “The instability of the steady flow past spheres and disks”. In: *J. Fluid Mech.* **254** (1993), pp. 323–344. DOI: 10.1017/S0022112093002150.

[90] Jacob Page and Rich R Kerswell. “Searching turbulence for periodic orbits with dynamic mode decomposition”. In: *J. Fluid Mech.* **886** (2020), A28. DOI: 10.1017/jfm.2019.1074.

[91] Abu Seena and Hyung Jin Sung. “Dynamic mode decomposition of turbulent cavity flows for self-sustained oscillations”. In: *Int. J. Heat Fluid Flow* **32** (2011), pp. 1098–1110. DOI: 10.1016/j.ijheatfluidflow.2011.09.008.

[92] Shervin Bagheri. "Koopman-mode decomposition of the cylinder wake". In: *J. Fluid Mech.* **726** (2013), pp. 596–623. DOI: 10.1017/jfm.2013.249.

[93] Jonathan H. Tu et al. "On Dynamic Mode Decomposition: Theory and Applications". In: *J. Comput. Dyn.* **1** (2013), pp. 391–421. DOI: 10.3934/jcd.2014.1.391.

[94] Bingni W. Brunton et al. "Extracting spatial-temporal coherent patterns in large-scale neural recordings using dynamic mode decomposition". In: *J. Neurosci. Methods* **258** (2014), pp. 1–15. DOI: 10.1016/j.jneumeth.2015.10.010.

[95] James M. Kunert-Graf et al. "Extracting reproducible time-resolved resting state networks using dynamic mode decomposition". In: *Front. Comput. Neurosci.* **13** (2018), p. 343061. DOI: 10.1101/343061.

[96] Deepthi Praveenlal Kuttichira et al. "Stock price prediction using dynamic mode decomposition". In: *2017 International Conference on Advances in Computing, Communications and Informatics, ICACCI 2017*. Institute of Electrical and Electronics Engineers Inc., 2017, pp. 55–60. DOI: 10.1109/ICACCI.2017.8125816.

[97] Jordan Mann and J. Nathan Kutz. "Dynamic Mode Decomposition for Financial Trading Strategies". In: *Quant. Finance* **16** (2015), pp. 1643–1655.

[98] Erik Berger et al. "Dynamic Mode Decomposition for perturbation estimation in human robot interaction". In: *IEEE RO-MAN 2014 - 23rd IEEE International Symposium on Robot and Human Interactive Communication: Human-Robot Co-Existence: Adaptive Interfaces and Systems for Daily Life, Therapy, Assistance and Socially Engaging Interactions*. Institute of Electrical and Electronics Engineers Inc., 2014, pp. 593–600. DOI: 10.1109/ROMAN.2014.6926317.

[99] Zhe Bai et al. "Dynamic mode decomposition for compressive system identification". In: *AIAA Journal* **58** (2020), pp. 561–574. DOI: 10.2514/1.J057870.

[100] Jessie Fanglu Fu et al. "Novel data-driven, equation-free method captures spatiotemporal patterns of neurodegeneration in Parkinson's disease: Application of dynamic mode decomposition to PET". In: *Neuroimage Clin.* **25** (2020), p. 102150. DOI: 10.1016/j.nicl.2019.102150.

[101] Christopher W. Curtis and Daniel Jay Alford-Lago. "Dynamic-mode decomposition and optimal prediction". In: *Phys. Rev. E* . **103** (2021), p. 012201. DOI: 10.1103/PhysRevE.103.012201.

[102] Yiyang Sun et al. "Biglobal instabilities of compressible open-cavity flows". In: *J. Fluid Mech.* **826** (2017), pp. 270–301. DOI: 10.1017/jfm.2017.416.

[103] Hrvoje Jasak. *Error Analysis and Estimation for the Finite Volume Method with Applications to Fluid Flows*. Tech. rep. 1996.

List of publications

Journal papers

- R. L. Agampodi Mendis, A. Sekimoto, Y. Okano, H. Minakuchi, and S. Dost, "Global Linear Stability Analysis of Thermo-solutal Marangoni Convection in a Liquid Bridge Under Zero Gravity," *Microgravity Science and Technology*, vol. 32, no. 4, pp. 729–735, 2020, ISSN: 18750494. DOI: 10.1007/s12217-020-09798-9.
- R. L. Agampodi Mendis, A. Sekimoto, Y. Okano, H. Minakuchi, and S. Dost, "The Relative Contribution of Solutal Marangoni Convection to Thermal Marangoni Flow Instabilities in a Liquid Bridge of Smaller Aspect Ratios under Zero Gravity," *Crystals*, vol. 11, no. 2, p. 116, 2021, ISSN: 2073-4352. DOI: 10.3390/cryst11020116.
- R. L. Agampodi Mendis, A. Sekimoto, Y. Okano, H. Minakuchi, and S. Dost, "A numerical study on the exact onset of flow instabilities in thermo-solutal Marangoni convection driven by opposing forces in a half-zone liquid bridge under zero gravity," *Journal of Chemical Engineering of Japan*, vol. 54, no. 8, pp. 1–7, 2021, DOI: 10.1252/jcej.21we041.

Conference proceedings

- R. L. Agampodi Mendis, A. Sekimoto, Y. Okano, and H. Minakuchi, "Global Linear Stability Analysis of Marangoni Convection Under Microgravity Conditions," The 31st Annual Meeting of The Japan Society of Microgravity Application (JASMAC-31), Mouri poster session, October 23-25 (2019), Sendai, Japan.
- R. L. Agampodi Mendis, A. Sekimoto, Y. Okano, and H. Minakuchi, "Global linear stability analysis of thermo-solutal Marangoni convection with the opposing forces under microgravity conditions," The 32nd Annual Meeting of The Japan Society of Microgravity Application (JASMAC-32), Mouri poster session, October 04-07 (2020), Online (ZOOM).

Awards

The 32nd Annual Meeting of The Japan Society of Microgravity Application (JASMAC-32), Mouri poster session, Outstanding Performance Award, Online (ZOOM), October (2020).

Acknowledgements

Completion of this thesis has been one of the most significant academic challenges I have ever had the encounter. Without the support, patience, and guidance of the following people, this task would not have been accomplished. It is to them that I owe my deepest gratitude.

I am really thankful to my supervisor Prof. Yasunori Okano for giving me his fullest support from the beginning. His advice and guidance were always helpful to me to complete this study. I am grateful to him for allowing me the opportunity to start my PhD researches at Osaka university and finish this thesis. I'm very delighted to have Prof. Okano as my supervisor.

I need thank to our assistant Professor Atsushi Sekimoto. He helped me a lot with much technical advice to improve my computer programming and research skills. Also, he supported me with supper computer configurations and administrative works during my study.

I would like to express my gratitude to Prof. Hisashi Minakuchi at Ryukus University. I appreciate his advice, discussion, and careful revision of my papers.

I would also acknowledge collaboration researches with Professor Sadik Dost at the University of Victoria, Canada. I appreciate his support to enhance my academic writing skills.

I wish to express thanks to all colleagues, Kelum Chamara, Islam Hassan, Daniel Cardoso Cordeiro, Petya Stoyanova, Wang Liya, Jin Chihao, Wang Lei, and other members of Okano Laboratory at Osaka University.

I want to thank the computational resources provided by Advanced Computational Scientific Program of the Research Institute for Information Technology at Kyushu University.

The research work was financially supported by the Nishimura Scholarship Foundation and Grant-in-Aid for Scientific Research (JSPS KAKENHI Grant No. JP19K22015) from the Ministry of Education, Culture, Sports, Science and Technology of Japan.

Last but not least I wish to avail myself of this opportunity, express a sense of gratitude and love to my beloved parents and my family for their manual support, strength, helps, and for everything throughout my life.